UC Irvine

UC Irvine Electronic Theses and Dissertations

Title

Advanced Catalyst Design for the Oxygen Reduction Reaction in Polymer Electrolyte Membrane Fuel Cells

Permalink

https://escholarship.org/uc/item/94b1d1tv

Author

Ly, Alvin

Publication Date

2022

Peer reviewed|Thesis/dissertation

UNIVERSITY OF CALIFORNIA, IRVINE

Advanced Catalyst Design for the Oxygen Reduction Reaction in Polymer Electrolyte
Membrane Fuel Cells

DISSERTATION

submitted in partial satisfaction of the requirements for the degree of

DOCTOR OF PHILOSOPHY

in

Materials Science and Engineering

by

Alvin Ly

Dissertation Committee:
Chancellor's Professor Plamen Atanassov, Chair
Associate Professor Iryna Zenyuk, Member
Assistant Professor Stacy Copp, Member

2022

DEDICATION

To my beautiful wife-to-be,

Thank you for continually supporting my dreams and ambitions

To my all-loving parents,

Thank you for allowing me to become the best version of myself that I can be

To my warmhearted grandparents,

I am forever gracious and owe my life's direction to the care that you gave me in my youth

To my friends and lab-mates,

I appreciate all the laughs and experiences and will cherish the memories eternally

TABLE OF CONTENTS

iii

LIST OF FIGURES

ACKNOWLEDGEMENTS

VITA

Alvin Ly

EDUCATION

2016   B.S. in Geology, University of California, Los Angeles

2018   M.S. in Materials Science and Engineering, University of California, Irvine

2022   Ph.D. in Materials Science and Engineering, University of California, Irvine

PUBLICATIONS

Ly, A., Asset, T., & Atanassov, P. (2020). Integrating nanostructured Pt-based electrocatalysts in proton exchange membrane fuel cells. Journal of Power Sources, 478, 228516. https://doi.org/10.1016/j.jpowsour.2020.228516

Chen, Y., Huang, Y., Xu, M., Asset, T., Yan, X., Artyushkova, K., Kodali, M., Murphy, E., **Ly, A.**, Pan, X., Zenyuk, I. V., & Atanassov, P. (2022). Catalysts by pyrolysis: Direct observation of transformations during re-pyrolysis of transition metal-nitrogen-carbon materials leading to state-of-the-art platinum group metal-free electrocatalyst. Materials Today, 53, 58–70. https://doi.org/10.1016/j.mattod.2022.01.016

Guo, S., Liu, Y., Murphy, E., **Ly, A.**, Xu, M., Matanovic, I., Pan, X., & Atanassov, P. (2022). Robust palladium hydride catalyst for electrocatalytic formate formation with high CO tolerance. Applied Catalysis B: Environmental, 316, 121659. https://doi.org/10.1016/j.apcatb.2022.121659

Murphy, E., Liu, Y., Matanovic, I., Guo, S., Tieu, P., Huang, Y., **Ly, A.**, Das, S., Zenyuk, I., Pan, X., Spoerke, E., & Atanassov, P. (2022). Highly Durable and Selective Fe- and Mo-Based Atomically Dispersed Electrocatalysts for Nitrate Reduction to Ammonia via Distinct and Synergized NO2– Pathways. ACS Catalysis, 12(11), 6651–6662. https://doi.org/10.1021/acscatal.2c01367

Ly, A., Asset, T., Murphy, E., Khedekar, K., Huang, Y., Xing, L., Xu, M., Wang, H., Chattot, R., Pan, X., Zenyuk, I., & Atanassov, P. (2022). Insights onto the Decorrelated Effect of Structural Defects and Local Coordination through the Use of Platinum Nanoflowers for the Oxygen Reduction Reaction. *In Preparation*.

Ly, A.*, Murphy, E.*, Wang, H.*, Asset, T., Huang, Y., Liu, Y., Guo, S., Pan, X., Zenyuk, I., & Atanassov, P. (2022). Electrochemical Trends of a Hybrid Platinum and Metal-Nitrogen-Carbon Catalyst Library for the Oxygen Reduction and Carbon Monoxide Oxidation Reactions. *In Preparation*.

CONFERENCES

Electrochemical Society 240th Meeting: *"Platinum Nanoflowers: A New Class of Nanostructured Electrocatalysts for the Oxygen Reduction Reaction"*. (2021)

Electrochemical Society 241st Meeting: *"Electrochemical Trends of M-N-C Materials as Catalysts and Active Supports for the Oxygen Reduction Reaction"*. (2022)

ABSTRACT OF THE DISSERTATION

Advanced Catalyst Design for the Oxygen Reduction Reaction in Polymer Electrolyte
Membrane Fuel Cells

by

Alvin Ly

Doctor of Philosophy in Materials Science and Engineering

University of California, Irvine, 2022

Chancellor's Professor Plamen Atanassov, Chair

With increasing global energy demand and energy-related carbon emissions, the
transportation sector (accounting for over 25% of total greenhouse gas emissions in the United
States) must be pushed towards total decarbonization. The polymer electrolyte membrane fuel
cells (PEMFC) are a promising energy conversion technology towards the zero-emission goals in
transportation applications. However, the high prices and short life cycles of the electrocatalytic
materials hinder the widespread commercialization of PEMFCs. Specifically, the design of the
cathode catalyst materials (driving the sluggish cathodic oxygen reduction reaction) is instrumental
in the success of PEMFCs. Current industry standards utilize a high platinum content catalyst (in
nanoparticle form) supported on carbon blacks. The understanding and development of the ideal
catalyst layer is three-fold: (1) the nanoparticle-ionomer interface, (2) the nanoparticle-support
interface, and (3) the ionomer-support interface. The first portion of my work outlines the ideal
cathodic catalyst layer based on a review of recent works which encompasses all three interfacial
interactions. The second portion of my work addresses the solid-state integration challenges (i.e.,
the nanoparticle-ionomer interactions) for the advanced structured Pt-based nanomaterials. The

final portion of my work addresses the next generation design parameters of carbon-based supports

with a focus on nanoparticle-support interactions.

1. Introduction

The transportation sector in the United States consumes the largest fraction of fossil fuels and emits the largest fraction of greenhouse gases.[1,2] Electrification of this sector can resolve some of the issues with Earth's depleting nonrenewable resources and risk of global warming. Combustion engines are inefficient and currently the most promising replacements are secondary batteries (Li-ion) and low temperature fuel cells (polymer electrolyte membrane fuel cells or proton exchange membrane fuel cells, PEMFCs).
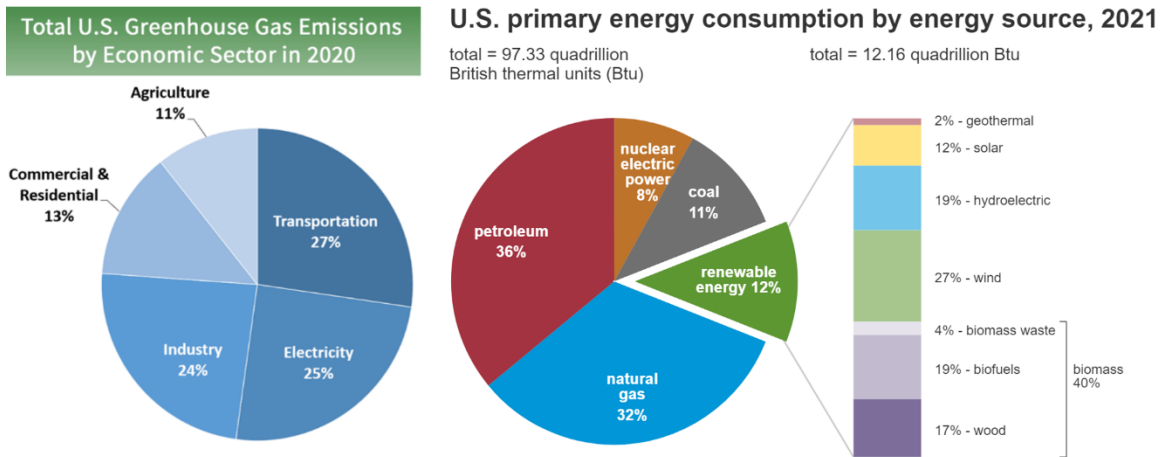
Fig 1.1 – Total U.S. greenhouse gas emissions by sector (from U.S. Environmental Protection Agency, 2020) and U.S. primary energy consumption by source (from U.S. Energy Information Administration, 2021)

1.1 Polymer (or Proton) Electrolyte Membrane Fuel Cell

The polymer electrolyte membrane fuel cell (PEMFC) is an electrochemical energy conversion device with a sandwich style basic building block known as a membrane electrode assembly (MEA). The MEA consists of a polymer electrolyte membrane in the center (typically Nafion) followed by the anode and cathode catalyst layers, gas diffusion layers, and

flow field plates as we move further away from the center. Hydrogen gas is fed to the anode side (allowing for the hydrogen oxidation reaction to occur) while oxygen gas is fed to the cathode side (allowing for the oxygen reduction reaction to occur) and the only by-product of the reactions is pure water. Typical applications for this type of device are used mainly in the transportation sector for passenger or cargo hauling purposes with benefits in decarbonization as well as possibly reducing the fueling requirements, especially for large-scale transportation (i.e., trucks and ships).
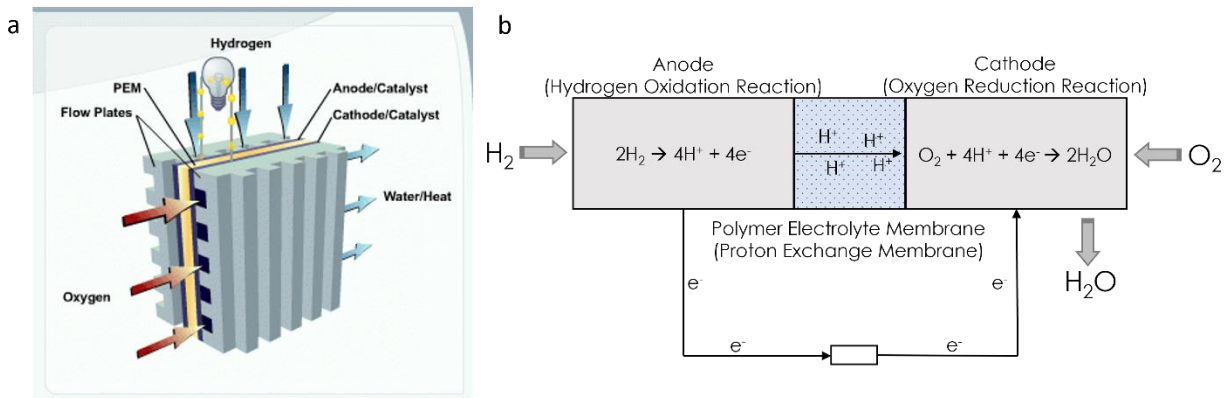
Fig 1.2 – Polymer electrolyte membrane fuel cell (PEMFC) structure: (a) symmetrical sandwich structure of the membrane electrode assembly (MEA) (from U.S. Department of Energy) and (b) species transport in catalyst layers during operation.

1.2 Technological and Economical Challenges

The widespread commercial deployment of PEMFCs is currently limited by the performance, stability, and cost. Platinum-based materials are utilized as state-of-the-art catalysts for both the anode and the cathode layers; however, the scarcity and cost of these materials are not offset by their performance and stability.[3,4] Emerging catalyst materials (namely metal-nitrogen-carbon based materials) provide much cheaper alternatives to

platinum-based catalysts, however, at the compromise of performance and durability.[5] The field must decide between the advancement of either platinum-based (PGM) or platinum-group-metal-free (PGM-free) catalysts as this may dictate the future of PEMFC-based vehicles. The benefits to using PGM catalysts include higher performance, longer durability, and partial commercialization in-place (due to previous deployments or developments of PEMFC vehicles, namely from Toyota, Hyundai, Daihatsu, and Nikola). Vehicles developed with PGM materials can expect to last longer with more performance consistency across different vehicles. The benefits to using PGM-free catalysts include cheaper costs and reduced need for extracting materials from used fuel cells. Vehicles developed with PGM-free materials can expect to degrade quickly, resulting in the need for swapping engine parts more frequently, however due to the quick production and cheap cost of the fuel cell materials, this should not be a major roadblock issue. Another issue (which will not be discussed in detail here) is the hydrogen economy, as the pipeline infrastructure of most countries are built for hydrocarbon transport (which can be also used for hydrogen transport) and would be competing fuel sources.
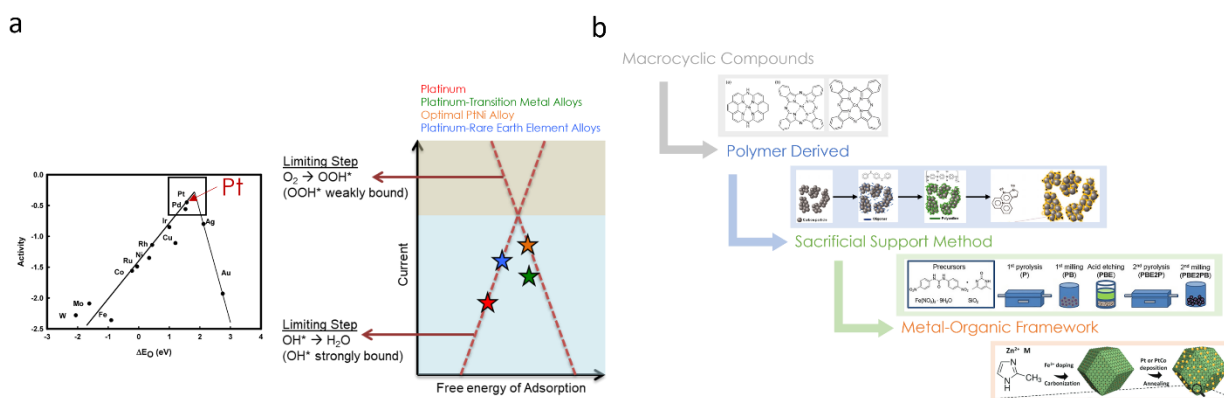
Fig 1.3 – Development of platinum-based and platinum-group-metal-free (PGM-free) catalysts: (a) volcano plot for the ORR activity of various elements and the limiting steps for the improvement of ORR activity, and (b) history of metal-nitrogen-carbon based catalysts.[10,11,14,26,31]

1.3 Hydrogen Oxidation Reaction (Anode)

The hydrogen oxidation reaction (HOR) occurs at the anode catalyst layer where the fed hydrogen gas is split into protons and electrons. The protons travel across the polymer electrolyte membrane (Nafion) and the electrons travel through an external circuit reaching the cathode catalyst layer. This reaction is typically catalyzed by a very low weight loading Pt/C catalyst, however recent works have shown M-N-C materials (particularly Pt-N-C) to be just as effective for the HOR.[6] As a result, the HOR is typically ignored in the development of PEMFCs as this reaction has very quick kinetics and is not the limiting factor in performance, durability, or cost for the overall fuel cell.

$$2H_2 \rightarrow 4H^+ + 4e^-$$

$$E_0 = 0.0V \text{ vs. RHE}$$
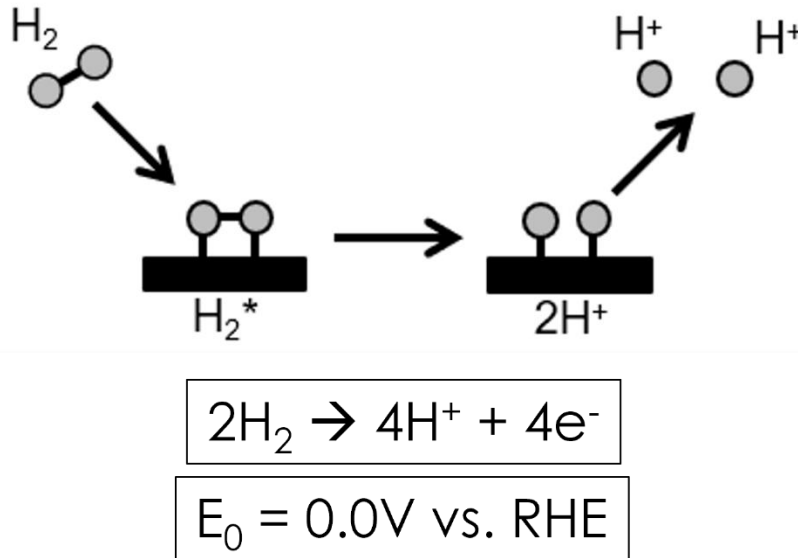
Fig 1.4 – Hydrogen oxidation reaction mechanism: the hydrogen molecule reaches active site on the surface of the catalyst and breaks apart to form protons and electrons.

1.4 Oxygen Reduction Reaction (Cathode)

The oxygen reduction reaction (ORR) occurs at the cathode catalyst layer where the fed oxygen gas must meet with the protons (transferred across the membrane) and the electrons (transferred through the external circuit and the conductive support material), from the anodic reaction, at the catalyst active site to form water. This reaction can typically occur with the desired $4e^-$ process (resulting in only the formation of water) or an undesired $2e^- + 2e^-$ process (resulting in a partial fractionation of products as hydrogen peroxide and water).[7,8] The cathodic ORR is a much more complex reaction than the anodic HOR, thus making it the limiting factor in a hydrogen-based fuel cell. Currently, the best material for catalyzing the ORR is platinum and still requires a significant amount of material in the cathode catalyst layer to reach the necessary performance. The industry standard platinum catalysts are typically small nanoparticles (~2-5 nm in diameter), although in recent decades, work has been done in further improving the activity of platinum-based nanoparticles through a variety of methods. These methods can be further divided into two categories: the order-based approaches and the disorder-based approaches, which will be discussed later in this work.[9] Another class of catalysts (known as metal-nitrogen-carbon or M-N-C catalysts) has been quickly progressing in the field of electrocatalysis, especially for the use of catalyzing the ORR and the development of this type of catalyst will also be discussed later in this work.[5,10,11]

$$O_2 + 4H^+ + 4e^- \rightarrow 2H_2O$$

$$E_0 = 1.229V \text{ vs. RHE}$$
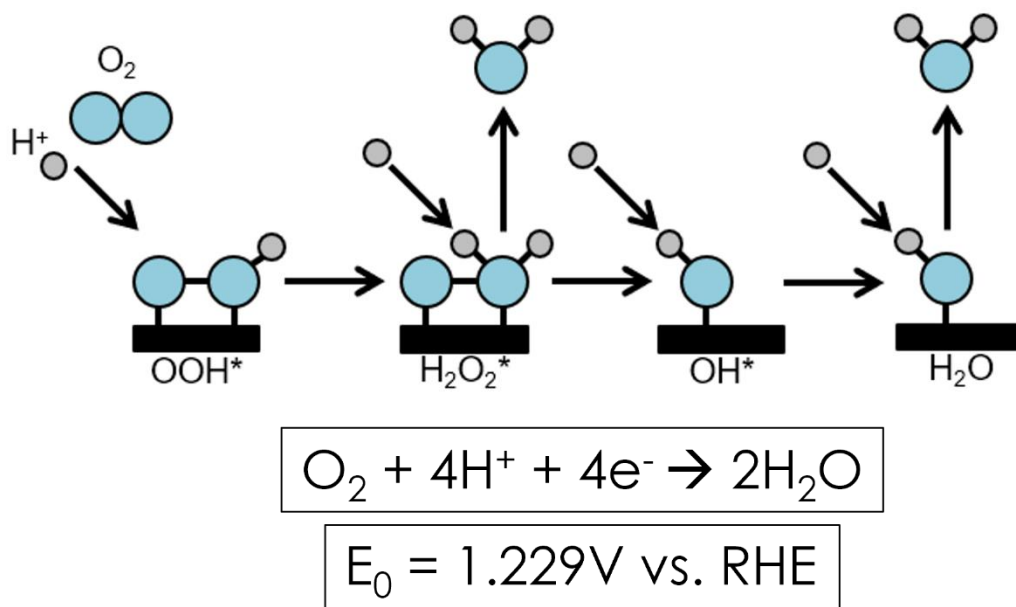
Fig 1.5 – Oxygen reduction reaction mechanism: the oxygen molecule reaches the active site along with the protons and electrons transported from the anode and is reduced to form water in a 4e⁻ or 2e⁻ + 2e⁻ transfer method.

1.5 Catalyst Support Materials

The analysis and study of catalyst support materials is out of the scope of this work; however, the topic should be briefly introduced. The most commonly used support material are carbon blacks (but typically Vulcan XC-72 made by Cabot Corp.), which can have varying degrees of surface area, porosity, graphitization, defectivity, and surface functionalization.[12] The combination of these factors can determine the overall effect that the carbon support has onto the catalyst layer by influencing particle anchoring, ionomer anchoring, and catalyst layer degradation. Many of these characteristics can also have inverse effects with the others, such as the increase of graphitization typically leading to the decrease of surface area and porosity. Research has also been done in incorporation of transition metal-oxide materials as support materials for platinum-based nanoparticles.[13,14] The benefit of these materials is their stability

in the acidic conditions and the operating potentials; however, the metal-oxides are typically plagued with poor nanoparticle-surface anchoring properties (including dispersity and agglomeration) as well as poor electrical conductivity. As a result, the majority of the field has moved towards development of modified carbon-based materials including the N-doping of carbons to improve nanoparticle and ionomer contact properties, improved graphitization in specific zones to improve operating stability, and the usage of ORR-active carbonaceous materials to increase performance of the catalyst layer.[15–18]
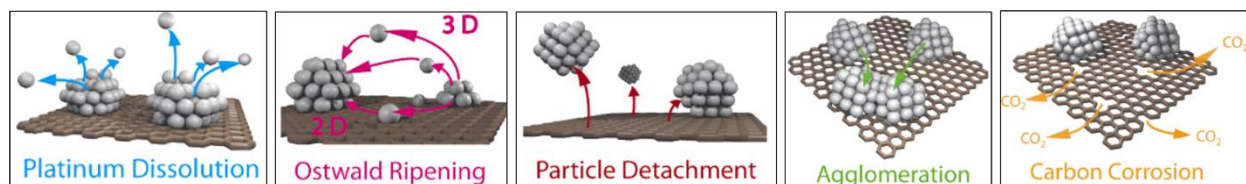
Fig 1.6 – Catalyst degradation mechanisms: platinum dissolution, Ostwald ripening, nanoparticle detachment, nanoparticle agglomeration, and carbon support corrosion.[19]

1.6 Catalyst Degradation Behavior

Typical catalyst degradation behaviors for platinum-based catalysts can be classified as effects from the active nanoparticles or the support materials. Phenomenon that affects the nanoparticles are mainly based upon platinum dissolution or particle movement (resulting in Ostwald ripening, agglomeration, and detachment).[19,20] Groups have been able to take advantage of alloying materials (specifically sub-surface gold) to significantly reduce the platinum dissolution rates during operation without activity losses, although the implementation of these core-shell based structures have yet to be seen in a fuel cell test.[20] The incorporation of N-dopants and F-dopants have shown promise in the strengthened anchoring the platinum nanoparticles to the carbon surface and could be the key to mediating particle

movement.[9,21,22] Phenomenon that affects the carbon support is mainly carbon corrosion in the operating potentials of the fuel cell (especially during the start-up and shut-down phases of the operation).[23] The typical design parameter to improve carbon corrosion durability is the increase of the graphitization of the carbonaceous material, however there is an inverse relationship between the accessible surface area (for nanoparticle anchoring) and the amount of graphitization.[23–25] As the higher Pt weight loaded samples fare better in fuel cell tests (due to less transport losses), the increase of carbon corrosion resistance by graphitization typically leads to activity losses. Both classifications of degradation behavior are still currently under intensive study by groups around the world as the stability of the fuel cell is one of the main hurdles prior to commercial deployment. The usage of M-N-C type catalysts introduce new degradation behaviors such as metal site dissolution, metal site agglomeration, and peroxides production in addition to current issues of carbon corrosion.[5,7,8] Advances have been made in mediating the peroxide production with the inclusion of ultra-low loading of Pt as peroxide scavengers, however the more work must be done on the specific design of the carbonaceous structure in order to improve catalyst durability.
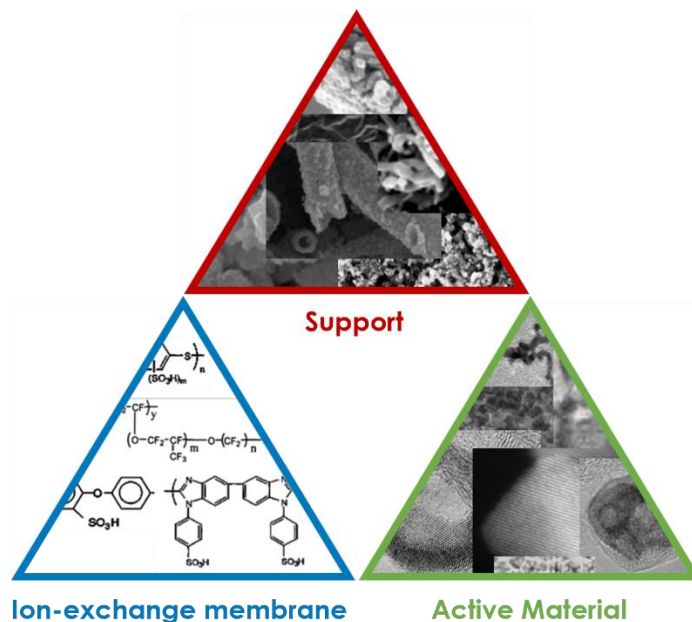
Fig 1.7 – The development of PEMFCs is primarily focused on three fronts: the ion-exchange membrane, the nanoparticle support material, and the active material. (adapted from Tristan Asset, "Catalyst Layers for Proton Exchange Membrane Fuel Cells", Seminar, UC Irvine, 2020)

1.7 Dissertation Focus

The focus of this work is three-fold: (1) to review the current stage of the field and offer an opinion on the direction of research that would seem most fruitful, (2) to investigate the incorporation of advanced nanoparticle structures within the current device architecture to understand the limitations of catalyst development, and (3) to understand the important interfacial phenomenon and interactions which occurs between the support material, active material, and ion-conducting material. In chapter 2, an explanation of relevant experimental methods and techniques and how they were applied to this work can be found. In chapter 3, the integration of advanced platinum-based nanostructures in polymer electrolyte membrane fuel cells is discussed including a short literature review as well as an opinion given on the ideal cathodic catalyst layer. In chapter 4, the novel platinum nanoflower structure is studied

and integrated into an MEA and its improvements and drawbacks are discussed in comparison to industry standard catalysts. In chapter 5, the modification of the carbon support by incorporation of M-N-C materials in a hybrid Pt/M-N-C catalyst format is explored and periodic table trends are presented for the ORR, CO oxidation reaction, and catalyst lifetime longevity. Finally, in chapter 6, the main conclusions for our work are presented as well as an outlook discussed looking towards the future of advanced catalysts for the oxygen reduction reaction.

2. Experimental Methods and Techniques

2.1 Synthesis of Platinum-based Nanoparticles and Nanostructures

Our nanoparticle synthesis methods are adapted from a traditional "polyol" method for solution-phase growth with a modern heating method of controlled microwave radiation. The polyol method refers to a synthetic method in which metal precursors are suspended in a glycol-based solvent and the solution is heated to a specific temperature for metal reduction and nanoparticle seeding and growth. This simple technique produces highly uniform nanoparticles of both mono and multi-metallic components with little to no agglomeration and contamination as the polyol solvent acts as the solvent, reducing agent, and ligand in the process. Traditional heating mechanisms of liquid or solid baths and heating mantles require multiple hours of heating (if not full days), however microwave-assisted heating can dramatically reduce this time to just a few minutes (allowing for energy conservation as well as improving the nanoparticle quality). Initial reports of microwave-assisted heating utilized household microwaves (both modified and unmodified), however more recent reactors have been developed to apply constant or pulsed radiation, monitoring solution temperature and vessel pressure, and including safeguards for operator safety. Our specific microwave reactor

is manufactured by CEM Corporation (MARS 6 Synthesis Reactor) and allows for temperature monitoring and large batch (liter-scale) production.

2.1.1 Platinum Nanoparticles

The bread-and-butter catalyst, the Pt nanoparticle, is made by incorporating an amount of a platinum chloride salt (either $PtCl_4$ or $H_2PtCl_6 * 6(H_2O)$) in ethylene glycol and then adjusting the solution pH to 10-12 by addition of an aqueous NaOH solution. The transparent, yellow solution is then placed in the microwave reactor vessel, heated immediately to 180°C (5 min ramp, 20 min hold), and allowed to cool to room temperature (~15-30 min). The resulting black solution is poured into a beaker, adjusted to pH 2-3 by addition of H_2SO_4, and ready to be combined with any nanoparticle support. When the support material (typically carbon black) is combined, the solution must be stirred for a minimum of 24 hours to allow for attachment, vacuum filtered, and dried at 60-80°C overnight. The basic pH adjustment prior to heating allows for the ethylene glycol to more efficiently reduce the metal precursor whereas the acidic pH adjustment slows further reduction (which causes more growth and agglomeration of nanoparticles) and shifts the platinum surface charge to be attractive towards a carbon support surface.

2.1.2 Platinum Nanoflowers

Our novel platinum nanoflower catalyst was created from a combination of recipes and techniques found in literature. An amount of a platinum chloride salt (either $PtCl_4$ or $H_2PtCl_6 * 6(H_2O)$), excess potassium iodide (minimum 6:1 mol ratio of iodide to platinum), and excess polyvinylpyrrolidone is added to ethylene glycol and stirred vigorously until dissolved. The originally transparent, yellow solution of the platinum salt in ethylene

11

glycol quickly changed to a transparent, red solution indicating the shift from chloride coordination to iodide coordination. The solution is then placed in a microwave reactor vessel, heated to 180°C (4 min ramp, 2 min hold), and allowed to cool to room temperature. The resulting black colloid solution is centrifuged in the first cycle with acetone followed by successive centrifugations (minimum 2 extra cycles) in minimal ethanol and maximal hexanes to purify and clean the nanoparticles. It should be noted that although the nanoparticles at this point are as "clean" of heavy organics at this point, the surface of the nanoflowers is still coated with these organics and must be removed in a later procedure. The nanoflowers are then dispersed and stirred in a water/ethylene glycol mixture with the carbon support added until vacuum filtration.

2.1.3   Platinum Alloy Nanoparticles

Platinum and transition metal alloy nanoparticles were synthesized in the same fashion as typical platinum nanoparticles with the addition of the transition metal salt precursor ($NiCl_2$, $CuCl_2$, $CoCl_2$…etc). The pH conditions and heating temperature remain identical; however, the heating times were optimized per alloying element (from 5 min hold to 25 min hold). Additionally, higher order multimetallic (3+ elements) were also synthesized using the same procedure without issues. An observation to be noted is that the nanoparticles are typically smallest (in diameter) when made monometallic and slightly increase in size with the increasing number of alloying elements.

2.1.4   Other Platinum-based Nanostructures

Although outside of the scope of this dissertation work, we have also been able to adapt and reproduce previously published syntheses of PtNi octahedra, PtCu octahedra, and PtNi

nanocubes with our microwave-assisted polyol method. The PtNi octahedra was made by combining an amount of $Pt(acac)_2$, $Ni(acac)_2$, and PDDA solution in ethylene glycol and sonicating/stirring until dispersed. An issue to note here is that the acetylacetonate precursors do not dissolve well into water or ethylene glycol, however this does not cause in issue in the synthesis so long as the large chunks are broken up into a finer dispersion. This solution is then placed in a microwave heating vessel, heated to 180°C, cooled to room temperature, and combined with a support material. The PtCu octahedra was made in the same fashion as the Pt nanoflowers with the addition of $CuCl_2$.

2.2 Synthesis of Carbon-based Support Materials

The most widely used support material is typically a commercially created carbon black (i.e. Vulcan, Ketjenblack, and Acetylene Black carbons). The advantages of commercially made carbons are its availability, ease of use, and quality control. However, in recent years, there has been a major research thrust into "designer" carbon supports with different dopants (both metallic and non-metallic elements) for added stability or activity of the catalyst.

2.2.1   Commercially Available Carbon Supports

Our main standard carbon has been the Vulcan XC-72R (R denoting the pre-ground powder form of XC-72) by Cabot Corporation because of its mesopore structure and relatively high surface area. Samples and testing was also completed with Ketjenblack EC-600JD, however the workability of the powder was poor and resulted in less accurate weight loading targets.

2.2.2   Nitrogen Doped Carbon Nanospheres

The majority of our N-doped carbon nanospheres were obtained through a collaboration with the Colorado School of Mines (Pylypenko Research Group). These nanospheres were synthesized through modified solvothermal method based on a previously reported sol-gel synthetic method. Generally, an amount of resorcinol was dissolved in an aqueous ethanol solution. A varied amount of ethylenediamine was added to the solution under stirring followed by the addition of formaldehyde. After 24 hours, stirred was ceased and the solution was heated in a sealed vessel to 100°C for an additional 24 hours. The resulting polymerized nanospheres were isolated by centrifugation and air-dried overnight. The dried material was ground to a fine powder and pyrolyzed under N_2 atmosphere up to 600°C - 900°C creating the final nitrogen doped carbon nanosphere product.

2.2.3 Atomically Dispersed Metal-Nitrogen-Carbon Materials

The metal-nitrogen-carbon material as a non-precious metal catalyst for the ORR has been a staple in our research group in the last decade. Detailed synthesis conditions and extensive characterization has been reported in previous works and is out of the scope of this work. Briefly, the metal precursors are combined with a silica of varying surface area and nicarbazin. Ultrapure water is then added to the mixture and sonicated to produce a viscous slurry, which is then stirred on a hotplate until dry. The remaining solids are ground and ball-milled to obtain a fine powder for pyrolyzing. The first pyrolysis step (for carbonization and structure formation) is performed at a specific temperature (typically either 650°C or 975°C) and a specific atmosphere (typically either H_2, Ar, or NH_3). The resulting powder is etched in an aqueous HF solution (for removal of the silica) and washed

to neutral pH. Then the material undergoes a second pyrolysis step (for etching remaining nanoparticles) in a similar fashion as the first step followed by a final ball-milling.

2.3 Physical Characterization

Due to the nature of our work (i.e. working with nanomaterials), physical characterization is exceptionally important to our materials development process. Viewing and analyzing the nanoscale structure of our materials is critical to the understanding of their catalytic performance.

2.3.1 X-Ray Diffraction

X-ray diffraction (XRD) is a crystallographic analysis technique based on the principle of the diffraction of X-rays by materials (specifically to identify crystalline materials). The typical diffraction tool is set up with 2 moving arms with an x-ray emitter at one end, an x-ray detector at the other end, and the powder (or thin film) sample sitting at the center. The emitter tube contains a hot filament that produces electrons which bombards a target (typically copper) dislodges an inner shell electron causing a characteristic x-ray to emit following the relaxation of an outer shell electron. The resulting x-rays are collimated and directed towards the sample. As the arms of the emitter and detector are raised, the intensity of the diffracted x-rays is recorded and when the geometry of x-ray paths satisfies the Bragg equation, constructive interference occurs and a peak appears in the detector. These peaks allow us to determine the crystal structure, identify the composition, and calculate the crystallite size of the sample. Typical experimental setups use a scan from ~5° to ~90° at speeds of 1° to 5°/min.

2.3.2 Electron Microscopy

Electron microscopy consists of techniques for obtaining high resolution images of samples in the micrometer to nanometer range. The two main types of electron microscopes are the scanning electron microscope (SEM) and the transmission electron microscope (TEM). These techniques are fundamentally different and produce different information about the structure of nanoscale materials.

In SEM, a beam of electrons is accelerated from the electron gun situated at the top of the sample column which is condensed through a series of lens before it reaches the sample surface. These electrons interact with the sample and produce signals from secondary electrons, backscattered electrons, diffracted backscattered electrons, photons, and heat. The most common imaging techniques take advantage of secondary electrons (showing sample morphology and topology) and backscattered electrons (showing compositional contrast). X-rays generated by inelastic collisions can also be useful for characterizing the chemical composition of the sample through energy dispersive x-ray spectroscopy (EDS). Typical SEMs can work with bulk, powder, or film samples and have working resolutions to tens of nanometers and are useful for surface level structure analysis.

In TEM, the beam of electrons is also emitted from the gun at the top of the sample column and condensed through a series of lens before reaching the sample surface. The beam then passes through the sample and either scatters or hits the screen at the bottom of the sample column. The electrons that come in contact with the sample are scattered (producing a dark shadow) and the background that has no interactions with the electrons remains as a bright background. Typical TEMs must only work with very thin samples that are deposited onto a supporting sample holder (called a grid) and have working resolutions

down to single nanometer scale and are useful for understanding the overall morphology of single particles since the images that are produced are the 2D projections of 3D materials.

Scanning transmission electron microscopy (STEM) is an additional technique in the TEM (combining the principles of SEM and TEM) and is also used with an additional detector, the high angle annular dark field (HAADF) detector. Like the SEM (and unlike traditional TEM), the electron beam is focused to a fine point and scanned across the sample in a raster pattern. The advantages of STEM include a higher resolution than SEM while allowing for spatially correlated data to be used (such as secondary electrons, backscattered electrons, characteristic x-rays, and electron energy loss). In STEM, the samples chemical composition and elemental interactions can be analyzed through EDS and electron energy loss spectroscopy (EELS). The typical dark sample and bright background (bright field imaging) is also possible along with the HAADF bright sample and dark background (dark field imaging) by capturing the backscattered electrons. The dark field imaging allows for much finer viewing of atomic structure whereas the bright field imaging allows for more spatial resolution of the sample.

2.3.3 Electron Tomography

Electron tomography (ET) is a technique in which a series of STEM or TEM images (which are in 2D) is stacked together to reconstruct a 3D image. This is exceptionally useful in the structural analysis of a single particle as we can reconstruct the inner porosities. First, an imaging tilt series ($\pm\,20°$ to $60°$) of a single area or particle is take in $1°$ or $2°$ increments. The resulting images are stacked in a program and adjusted by hand so that the axis of rotations of all images align perfectly. Then the program is run and the resulting tomogram

is displayed (representing the overlapping area of the imaged section). ET is a relatively new imaging processing technique and is very work intensive to obtain the reconstruction of a single particle but can display high resolution internal data in which no other imaging technique can.

2.3.4　Brunauer-Emmett-Teller Analysis

Brunauer-Emmett-Teller (BET) analysis utilizes the theory of physical adsorption of gas molecules onto a solid surface to measure the specific surface area of solid and porous materials. The main gas used for surface area analysis is N_2 and is completed at the boiling temperature of liquid nitrogen. Generally, the powder sample is loaded into a quartz tube that is evacuated at cryogenic temperatures. Then the nitrogen gas is dosed into the sample tube at controlled intervals and allowed to equilibrate. The weight of the nitrogen adsorbed is determined and the surface monolayer coverage can be calculated. Additionally, the micro and meso-pore volume and distribution are also measured through isotherm analysis by filling all pores with nitrogen and reducing the pressure incrementally.

2.4 Chemical Characterization

Chemical characterization methods are exceptionally important to hypothesizing and understanding the electrochemical behavior of the catalysts. Through these characterization techniques, we can control the total platinum amount and normal activity and performance values to the mass of platinum for consistent comparisons between catalysts. We can also analyze the atoms and species within the nanoparticle and on the surface to further correlate why activities may be higher or lower than a standardized catalyst.

2.4.1　Thermogravimetric Analysis

Thermogravimetric analysis (TGA) is a technique that determines the amount (by weight) of volatile components in a material as the sample is heated to a specific temperature at a constant rate. In this case, an amount of the sample (typically 5-10mg) is placed in an alumina crucible in the machine and the temperature is ramped from room temperature to 1200°C in an oxygenated atmosphere. The carbon support will be burned off throughout this process leaving behind just the platinum (and any additional metals used in the synthesis), which will give us the total platinum (or metal) weight loading for that sample.

2.4.2 Inductively Coupled Plasma – Mass Spectrometry

The inductively coupled plasmas mass spectrometer (ICP-MS) is a tool that determines the elemental composition of a liquid (typical operating mode) or solid (laser ablation mode) sample. In our case, the liquid sampling was what was usually used. By digesting a small amount of powder sample (~1-5 mg) in either aqua regia (if digesting metal nanoparticles supported on carbon) in a tabletop method or pure nitric acid (if digesting low metal weight loading samples) in a microwave reactor method, we can obtain a nitric acid-based solution that is further diluted by the correct factor. The diluted samples can now be used alongside a diluted standard sample (purchased directly from Inorganic Ventures) in the ICP-MS. Briefly, the sample is introduced to the chamber, passed through the generated plasma, and flows down the sample guide where elements are separated by weight.

2.4.3 Energy Dispersive Spectroscopy

Energy dispersive spectroscopy (EDS) is an elemental analysis technique typically coupled with electron microscopy (either SEM or TEM). The electron beam of the microscope interacts with the sample and causes characteristic x-rays to be released from your sample surface which can be interpreted by the detector into elemental counts. Generally, this technique is used for elemental identification rather than elemental quantification as the sampling size is quite limited and the resolution has some error.

2.4.4　X-Ray Photoelectron Spectroscopy

X-ray photoelectron spectroscopy (XPS) is also an elemental analysis tool which focuses on high precision atomic binding environment of the sample surface. In XPS, the sample is instead excited with x-rays which causes the sample surface to release electrons which can be measured by the detector. The energy of the measured electrons can give insight into the elemental composition of the sample surface as well as what type of binding the atoms have with each other (i.e., M-O, M-N…etc.). This technique is especially useful for understanding the catalytic active sites of the sample, as most of the catalytic sites occur on the surface of the sample and can be analyzed through XPS.

2.4.5　X-Ray Absorption Spectroscopy

X-ray absorption spectroscopy (XAS), typically split into the EXAFS (extended x-ray absorption fine structure) and XANES (x-ray absorption near edge structure) regions, is an elemental state analysis technique done usually in a synchrotron facility. XAS measures the transmission of x-rays as the x-ray energy is incrementally increased close to the absorption edge, which corresponds to the energy that is required to eject an electron from an atom in the sample. The first portion of the signal is XANES and can give

information on local oxidation states and binding symmetries. The second portion of the signal is EXAFS and can give information on coordination environment and chemical bond lengths. This tool is especially useful in the field of catalysts as we move towards single-atom catalysts and can identify the chemical environment of the active atom.

2.5 Electrochemical Characterization (Liquid Electrolyte)

The main performance characterization tool of our catalysts is the rotating [ring] disc electrode (R/RDE) assembly as it allows for rapid electrochemical measurements to obtain the intrinsic activities of the synthesized catalysts. The R/RDE testing protocol can be split into the following sections: catalyst ink and electrode tip preparation, cyclic voltammetry, linear sweep voltammetry, and degradation cycling.

For the ink suspension preparation, the catalyst powder is combined and ultrasonicated with a Nafion solution, ultrapure isopropyl alcohol, and ultrapure water in a way that we obtain an ionomer to carbon ratio of 0.3 and a final volume of 1-2 mL. The working electrode tip (PTFE based with a glassy carbon center disc and platinum ring) was cleaned thoroughly with successive washes in acetone, alcohol, and ultrapure water. If the glassy carbon disc developed excessive scratching or defects, the electrode tip would be sanded with Al_2O_3 polishing solutions prior to washing to maintain its glossy surface. The electrolyte was prepared in a volumetric flask by adding correct amounts of concentrated perchloric acid ($HClO_4$) and ultrapure water. This must be made fresh and used within a few hours to prevent degradation of the perchloric acid. Once the electrode tip is cleaned and the ink suspension is prepared, the ink was dropped onto the glassy carbon center disc under light rotation (100-400 rpm) to promote even drying.

Cyclic voltammetry (CV) was completed in N_2-saturated electrolyte to understand the surface reactivity of the tested catalyst. First, a set of 100 rapid scans (500 mV/s) was done from 0.05V – 1.23V to fully clean the surface of the platinum. Then a set of 3 slow scans (20 mV/s) was done in the same potential window to analyze the surface species. From the slow scans, we can extract the adsorption and desorption of H^+ (H_{upd}) and the formation and reduction of surface oxides. The desorption of H^+ allows us to calculate the electrochemically active surface area (ECSA) of the platinum as well as analyze the exposure of specific crystalline facets. Although rarely used in this fashion for the work presented here, it is also possible to do cyclic voltammetry in a CO-saturated then N_2-purged electrolyte to find the CO desorption peak. The CO oxidation peak is generally known to be a slightly more accurate representation of the true ECSA of the catalyst, however the usage of the toxic CO gas typically complicates the experimental setup significantly. In this work, CO oxidation is mainly used as an indicator for the active surface properties of the platinum-based nanoparticles as shifts in peak potential and peak intensity correlate to changes in species binding and reaction energetics.

The electrocatalytic activity for the oxygen reduction reaction was calculated through the linear sweep voltammograms. A slow (5 mV/s) sweep from 0.05V to 1.05V was done to allow for minimal capacitive currents and better representation of steady-state PEMFC conditions. A noteworthy observation is that a slow scan rate (5 mV/s) significantly depreciates the activity values by up to a factor of 2-5x when compared to slightly faster scan rates (20 mV/s to 50 mV/s) thus the slow scan rates tend to match the catalyst's intrinsic activities better.

The accelerated stress tests (ASTs) were done in the R/RDE setup through degradation or potential cycling. Two potential cycling windows are possible and target separate degradation

22

behavior. The first potential window represents a load-cycling protocol with a triangular potential wave pattern measuring from 0.6V to 1.0V at 50 mV/s to mimic the operational conditions that the PEMFC experiences. This range is known to target more of the Pt degradation mechanisms. The second potential window represents a start-stop protocol and is also done with a triangular potential wave pattern measuring from 1.0V to 1.5V to mimic the start-up and shut-down behavior of a PEMFC. This range is known to target more of the carbon support degradation mechanisms. The potential cycling scans can be done at elevated temperatures of 60° to 80°C, however for the work here, most of the ASTs were completed at room temperature to avoid damaging the PTFE working electrode tip where PEEK working electrode tips would be more resilient.

2.6 Electrochemical Characterization (Solid Electrolyte)

The final performance characterization tool is the fuel cell test station, which measure the performance of the catalyst through a membrane electrode assembly (MEA) setup. This process is time consuming and requires large amounts of catalyst powder per trial and is typically saved for the catalysts that have been proven to outperform standard catalysts in an R/RDE setup. The fuel cell testing protocol can be split into the following sections: MEA fabrication, break-in procedure, CO displacement, polarization curves, cyclic voltammetry, and accelerated stress test.

The ink suspension was made by adding the catalyst powder, Nafion solution, ultrapure isopropyl alcohol, and ultrapure water with an ionomer to carbon ratio of 0.6 to 0.8 in a small PTFE vial filled with zirconium oxide beads. The vial was sealed and ball-milled overnight to achieve a smooth dispersion. The ink suspension was then poured onto a sheet of PTFE and a metal rod with a specific height gap (100um to 800um) was used to push the ink liquid to form

a thin layer. This process was done twice, once for the cathode catalyst layer (catalyst to be analyzed) and once for the anode catalyst layer (standard Pt/C catalyst). A 5 cm^2 square was cut from both catalyst layer sheets and sandwiched with a Nafion membrane in between before hot pressing (150°C for 2 min) the layers together. The PTFE backings were peeled off the finished MEA and assembled into a Baltic fuel cell setup with a serpentine gas flow channels and Freudenberg gas diffusion layers (GDLs).

The MEA was broken in by holding at 0.3V, 0.6V, and 0.8V for 30s at each potential until the current density reached a steady state. After breaking the MEA, we could either begin the fuel cell testing (with polarization curves) or perform a CO displacement (or CO stripping) if needed. To perform the CO displacement, the CO gas was introduced to the cathode side while holding the potential at 0.1-0.35V. The gas was allowed to permeate the catalyst layer for a few minutes and then the cell was purged with nitrogen for at least 15 minutes. A cyclic voltammogram was then done between 0.05V to 1.23V to remove the CO from the surface of the catalyst and the CO oxidation peak was recorded. This entire procedure was repeated for a total of 3 times to ensure data accuracy and full CO coverage of the catalyst. Polarization curves were taken in either H_2/O_2 or H_2/Air (anode/cathode) environments by applying a current density (from 0 – 2000 mA/cm^2) and recording the potential of the cell (which was averaged over the period of data collection). The typical accelerated stress test was done by potentiostatic cycling of the cell (between 5,000 to 30,000 total cycles) from 0.6V to 0.95V (or OCV, whichever is the smaller value) using a square wave pattern. Full characterizations (polarization curve, CV, EIS) were performed at increments of 5,000 or 10,000 cycles. Although not completed in this work, it's also possible to test the accelerated degradation of

the carbon support by performing the same method but with the potentiostatic cycling between 1.0V to 1.5V.

3. Integrating Platinum-based Nanostructures in PEMFCs

Platinum-based nanomaterials remain one of the most effective options as proton exchange membrane fuel cell (PEMFC) cathode electrocatalysts for enhancing the sluggish kinetics of the oxygen reduction reaction (ORR). Their morphology has been greatly improved throughout the last decade, shifting from 2 – 3 nm nanoparticles (NPs) supported on carbon blacks to complex shaped nanostructures (such as nanoframes, octahedra, *etc*.). These nanostructures take advantage of electronic and structural effects, such as the (i) *strain-ligand effect* achieved through alloying, (ii) preferential crystallite orientation, or (iii) positive use of the structural defects. Improvement factors in specific activity of up to 60 have been achieved compared to classic Pt NPs in liquid electrolyte, however, such tremendous enhancements do not translate to solid electrolyte, *e.g.* in PEMFCs. Here, we discuss the PEMFCs-induced limitations for these complex electrocatalysts mainly evolving around the ionomer, *i.e.* Nafion®, which (i) exhibits a heterogenous dispersion onto the support surface, (ii) has difficulty impregnating the nanostructure's inner pores (for nanoframes or porous-hollow nanoparticles), and (iii) electrostatically interacts with Pt, therefore displacing the nanoparticles depending upon the PEMFC operation potential. We suggest several options in overcoming these challenges, including (i) functionalizing the support surface with nitrogen moieties, increasing the density of anchoring sites, and thus facilitating the nanostructure dispersion and (ii) initially encapsulating the nanostructures with well-defined ionic liquids and eventually replacing the Nafion® in the catalytic layer.

3.1 Introduction

Earth contains a finite amount of resources and one of the greatest challenges of humanity is how to use them without jeopardizing our future and maintaining a high standard of living. Transportation sector in the US consumes the largest fraction of fossil fuels, where combustion engines are highly inefficient and produce CO_2 emissions [26]. Electrification of transportation sector can resolve some of the issues associated with burning fossil fuels and currently the most promising replacement options are (i) secondary batteries, such as Li-ion, and (ii) low temperature fuel cells. This opinion letter discusses advances and challenges remaining to wide commercialization of fuel cell technologies and, more specifically, proton exchange membrane fuel cell (PEMFC) catalysts. The main electrochemical limitation of the PEMFCs is the sluggish kinetics of the cathodic reaction, the oxygen reduction reaction (ORR, $O_2 + 4H^+ + 4e^- \rightarrow 2H_2O$). Here, the best electrocatalysts are Pt-based [27], even though Pt binds the oxygen intermediates slightly too strongly, by approximately 0.1 eV [28,29]. Pt group metals (PGMs), however, are scarce in the Earth's crust and, because of their unequal geographic repartition (90% of the Pt is found in South Africa [30]), their extraction and use are heavily dependent upon the political geosphere.

Decreasing the platinum content in the PEMFC cathode is mandatory to achieving cost-effective broadly deployed fuel cell technologies. In that frame, one can either (i) use non-platinum group metals electrocatalysts, such as metal-nitrogen-carbon electrocatalysts [31–34] or (ii) reduce Pt loading without diminishing power densities. Platinum reactivity for the ORR is highly dependent of its electronic structure: its 5d-band density of states [35–38] and can be tuned using (i) *order*-based approaches by alloying [39–41] or changes in the electrocatalysts' surface

orientation [42,43] or (ii) *disorder*-based approaches, by varying the coordination number and the inter-atomic distances of active sites to optimize their reactivity for the ORR.[44–46]

Such concepts resulted in the synthesis of complex Pt-based electrocatalysts, such as octahedra [42], nanoframes [47], porous particles [48,49], and many others, far from the classic 2 – 3 nm Pt nanoparticles (NPs) supported on carbon (Pt/C) that was successfully implemented in PEMFCs during the last decade. Despite being extremely promising in liquid electrolyte, in which mass activity factors *vs.* Pt/C reached up to 20 (*e.g.* nanoframes [47]) to 60 (*e.g.* nanowires [50]), these new electrocatalysts have failed so far in achieving similar improvement factors in membrane electrode assemblies (MEAs) [51,52]. After discussing this new generation of Pt-based electrocatalysts, this opinion letter aims to provide an overview of the MEA-induced limitations and the eventual paths to overcome them.

3.2 New Generation of Electrocatalysts

As an element, Pt is the best electrocatalyst for the ORR. However, as mentioned in the introduction, it binds the oxygen intermediates (OH* and OOH*) *ca.* 0.1 eV too strongly [28,29]. To achieve an optimal binding strength, the Pt electronic structure must be slightly tuned. The different pathways to do so are represented in **Figure 1** and are divided into two categories*:* (i) the *order*-based approaches and (ii) the *disorder*-based approaches.
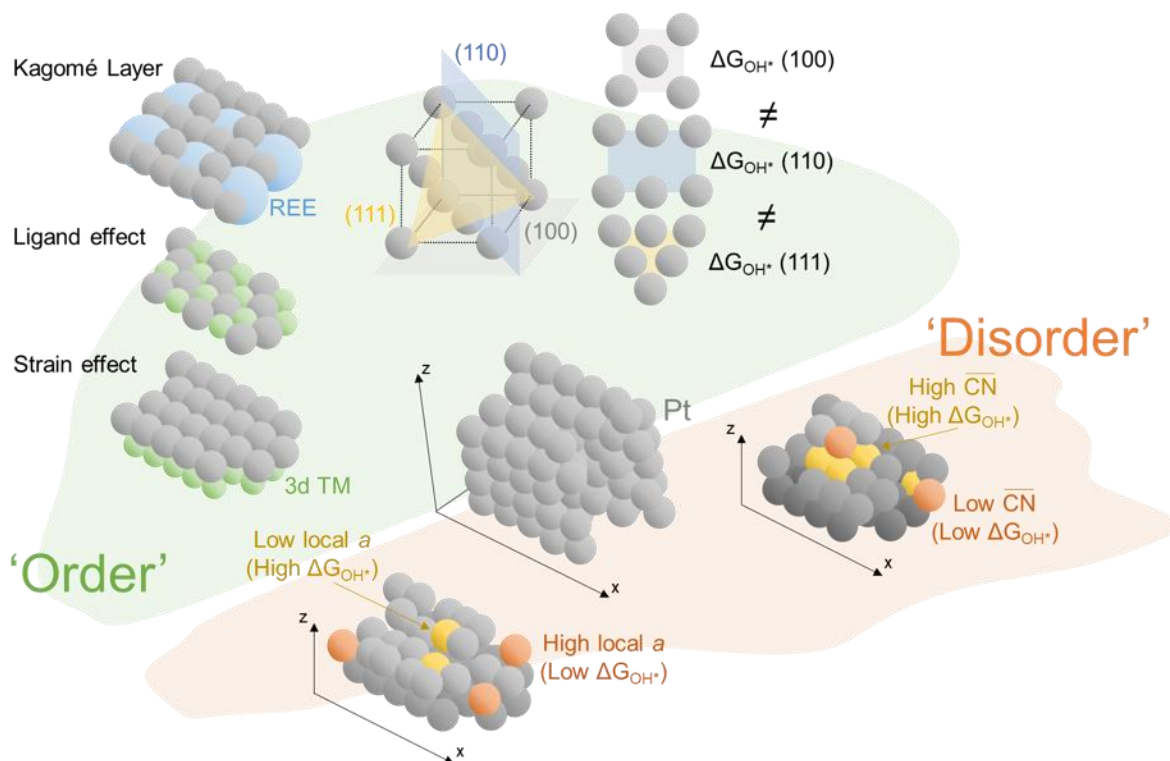
Fig 3.1 - Order vs. Disorder – the paths to improve the Pt-based catalysts activity. Schematic representation of the different strategies undergone to enhance the Pt-based electrocatalyst activity: (i) Order-based approaches, i.e. strain/ligand effect (with 3d transition metals – TM) and formation of a Kagomé layer through the use of rare-earth elements (REE); preferential orientation of the electrocatalyst surface; (ii) Disorder-based approaches, i.e. controlling the generalized coordination number and the local interatomic distance as a mean of tuning the OH$_{ads}$ strength on a given active site.

The former can be achieved by alloying platinum with another element, such as a 3d transition metal [53–56], or rare earth element [57–59], taking advantage of the *strain-ligand* effect. The *strain-ligand* effect (see **Figure 1**) modifies the platinum electronic structure by (i) contracting the Pt lattice through an addition of a sub-layer of 3d transition metal [39,40] (strain effect) or (ii) directly modifying the Pt electronic structure through the presence of neighboring 3d transition metal [60] (ligand effect). The ORR activity follows a volcano-type dependence to the alloying element, with Co, Ni, and Fe displaying the best behaviors [61]. This inspired the synthesis of bimetallic nanoparticles, with an improvement factor in mass activity of 2 – 3 *vs.*

traditional Pt NPs in liquid electrolyte (see **Figure 2**) [62]. Bimetallic NPs can be further tuned

by dealloying, resulting in core@shell NPs [63,64]. Their lattice strain and shell thickness can be

controlled through the nature of the alloying element and its initial abundance in the bimetallic

NPs. Ni@Pt and Co@Pt core@shell NPs exhibited improvement factors in mass activity of up

to 5 – 10 *vs.* traditional Pt NPs in liquid electrolyte (see **Figure 2**) [65]. It is also important to

address the stability of the core@shell and bimetallic NPs. Chemical treatments or *operando*

conditions (*e.g.* high potentials, low pH, *etc.*) result in NP roughening, nanopore formation,

and non-noble metal leaching, all of which can greatly affect the NPs morphology [56,66].
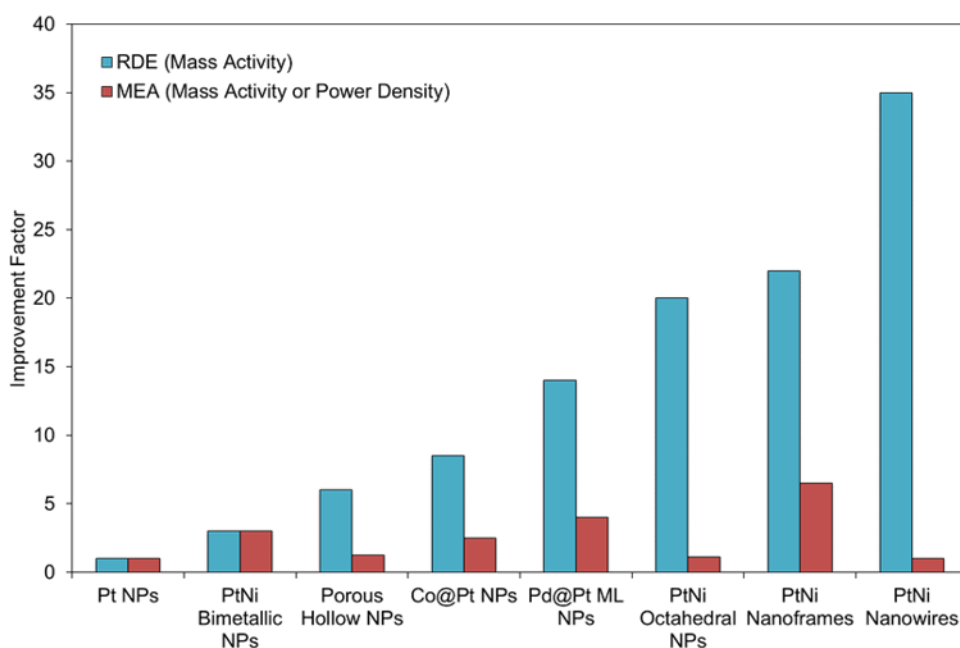
Fig 3.2 - Improvement factor in mass activity vs. traditional Pt nanoparticles; (i) traditional Pt NPs (RDE at 0.90 V vs. RHE, electrolyte: 0.1 M $HClO_4$, MEA at 0.90 V, see Stamenkovic and Markovic [37] for detailed conditions); (ii) bimetallic PtNi NPs (RDE at 0.95 V vs. RHE, electrolyte: 0.1 M $HClO_4$, scan rate; MEA at 0.90 V, see Stamenkovic et al. [37] and Han et al. [55] detailed conditions); (iii) core@shell NPs (RDE at 0.90 V vs. RHE, electrolyte: 0.1 M $HClO_4$, scan rate; MEA at 0.925 V, see Wang et al. [40] and Kongkanand et al. [56] for detailed conditions); (iv) Porous Hollow PtNi NPs (RDE at 0.90 V vs. RHE, electrolyte: 0.1 M $HClO_4$; MEA at 0.90 V, see Dubau et al. [24] and Asset [57] for detailed conditions); (v) Pt monolayer on Au@Pd cores (RDE at 0.90 V vs. RHE; MEA at 0.925 V, see Kongkanand et al. [56] for detailed conditions); (vi) Octahedral PtNi NPs (RDE at 0.9 V vs. RHE, electrolyte: 0.1 M $HClO_4$, scan rate: 50 mV/s; MEA at maximum power density, see Li et al. [44] for detailed conditions); (vii) PtNi nanoframes; (RDE at 0.95 V vs. RHE, electrolyte: 0.1 M $HClO_4$, scan rate: 50 mV/s; MEA at 0.90 V, see Chen et al. [22] and Stamenkovic et al. [37] for detailed conditions); (viii) Ultra-jagged nanowires (RDE at 0.90 V vs. RHE, electrolyte: 0.1 M $HClO_4$; MEA at 0.90 V, see Li et al. [25] and Mauger et al. [27] for detailed conditions).

29

As illustrated by Colic and Bandarenka [67], improvement of the ORR activity can also be achieved by alloying platinum with rare-earth elements, through the formation of a specific crystalline structure, the 'Kagomé' layer (see **Figure 1**), which increases the Pt strain and modifies its electronic structure and, thus, enhances its reactivity [57–59]. Another *order*-based approach relies on synthesizing electrocatalysts with complex, geometrical shapes, that expose specific crystalline facets (*e.g.* (111), (110), *etc.*), often referred to as the *ensemble* effect. As presented in **Figure 1**, each crystalline plane has a different atomic density and, therefore, a different binding strength toward OH* species [43,68]. Electrocatalysts driven by the *ensemble* effect include multi-pods, extended surfaces, or polyhedral nanoparticles (*e.g.* octahedra). The most promising catalysts, such as octahedral PtNi [42] and PtNi nanoframes [47], combine *strain* and *ensemble* effects. Octahedral PtNi NPs reported improvement factors from 5 to *ca.* 50 *vs.* traditional Pt NPs in liquid electrolyte [42,69,70], whereas PtNi nanoframes exhibited an improvement factor of *ca.* 20 [47] (see **Figure 2**). Since the *ensemble* effect relies on the nanostructure shape, it suffers from electrochemically-induced restructuring [66,71]. Additionally, these catalysts have radially non-isotropic shapes, thus creating complex interfaces with both the carbon support and the ionomer.

The *disorder*-based approach for ORR was first highlighted by Kuzume *et al.* [72] on extended surfaces. Stepped surfaces exhibited an increased specific activity *vs.* (111) surfaces [72–75], which was ascribed to a step-induced disturbance of the co-adsorbed OH* and OOH* network, resulting in a weakening of their adsorption strength next to the step [75]. Calle-Vallejo *et al.* [44] later evidenced that the variation of generalized coordination number, (that is, the coordination number of an active site calculated considering both its 1st and 2nd neighbors)

between an 'on the step' and an 'under the step' site induced this discrepancy in ORR intermediate binding strength, *i.e.* the 'under the step' site weakly binds OH*, thus presenting enhanced ORR kinetics, whereas the 'on the step' site strongly binds OH*, thus exhibiting lower kinetics for the ORR. According to Calle-Vallejo *et al.* [44], an ideal active site for the ORR should present a generalized coordination number of 8.3. Additional findings from Le Bacq *et al.* [46] indicated that, in addition to the generalized coordination number, the distance with the neighboring atoms was of critical importance, where a Pt atom in a closely packed structure would exhibit a weaker OH* binding than a Pt atom afar from its closest neighbors. Although a weaker binding often indicates higher activity, it is important to remember that Pt-based catalysts are bound to the Sabatier principle, *i.e.* an ideal catalyst should bind the intermediates species nor to strongly, nor too weakly. Hence, a Pt active site with a too high generalized coordination number, or too close to its nearest neighbors, also exhibits depreciated performances. Structural defects-based electrocatalysts exhibit jagged, stepped and/or polycrystalline structures, hence containing high coordination atoms and highly microstrained domains, the microstrain being the local variation of the global strain. A high microstrain indicates an electrocatalyst with lattice-strained and lattice-dilated domains, *e.g.* often due to their polycrystalline structure and the lattice dilation near grain boundaries [76,77].

Using *disorder*-based approaches, Li *et al.* [50] synthesized PtNi nanowires with an improvement factors of 7 *vs.* Pt traditional NPs. They reached *ca.* 50 after nickel dealloying, due to the formation of a jagged Pt nanowire surface (see **Figure 2**) [50]. Similar findings in liquid electrolyte were observed by Mauger *et al.* [52] Porous-hollow PtNi NPs (see **Figure 2**) and PtNi sponges were synthesized and reached mass activity improvements of 5 – 10 *vs.*

traditional Pt in liquid electrolyte [49,78,79]. However, similarly to the preferentially oriented electrocatalysts, these materials also exhibit much larger diameters (*ca.* 10 – 15 nm for the porous hollow PtNi NPs [49], 50 nm for the PtNi sponges [78], hundreds nm for the PtNi nanowires [50], *etc.*), and, thus, complex interfaces with the ionomer and the carbon supports, and 1 – 5 nm porosities , introducing transport challenges.

Increasing the nanostructure complexity results in side effects, either detrimental or advantageous. Originally, the shift from Pt extended surfaces to Pt NPs supported on carbon was undergone to increase the mass activity. The NPs optimal size was shown to be *ca.* 2 – 3 nm, as lower diameters result in NPs presenting mainly low coordination atoms and, thus, depreciated ORR activity [80], whereas larger NPs resulted in a large fraction of the Pt atoms being unutilized for the ORR. This is the case of the nanostructures described throughout this section as they exhibits diameters (except the bi-metallic NPs), ranging from 5 nm to 20 nm [42,47,49,63] (or hundreds, in the case of nanowires [50]). However, nanostructures such as core@shell [63], multilayered (*i.e.* Pt-monolayer on the NPs surface [54,81]) and hollow nanoparticles [49,82] optimize Pt utilization as the core, inactive atoms are 3d transition metals, Pd, Au, or simply void. Thus, platinum becomes localized at the reactive interface with the electrolyte. Some nanostructures, *e.g.* porous hollow PtNi NPs [49], nanoporous PtNi [83], *etc.* also exhibit an inner network of porosities, hence increasing their specific surface and presenting, in this network, concave sites with an increased generalized coordination number [44]. Unfortunately, the nanostructure's increased size, along with the eventual inner porous network, face their limitations when implemented in fuel cells, *i.e.* in drastically different conditions than in liquid electrolyte.
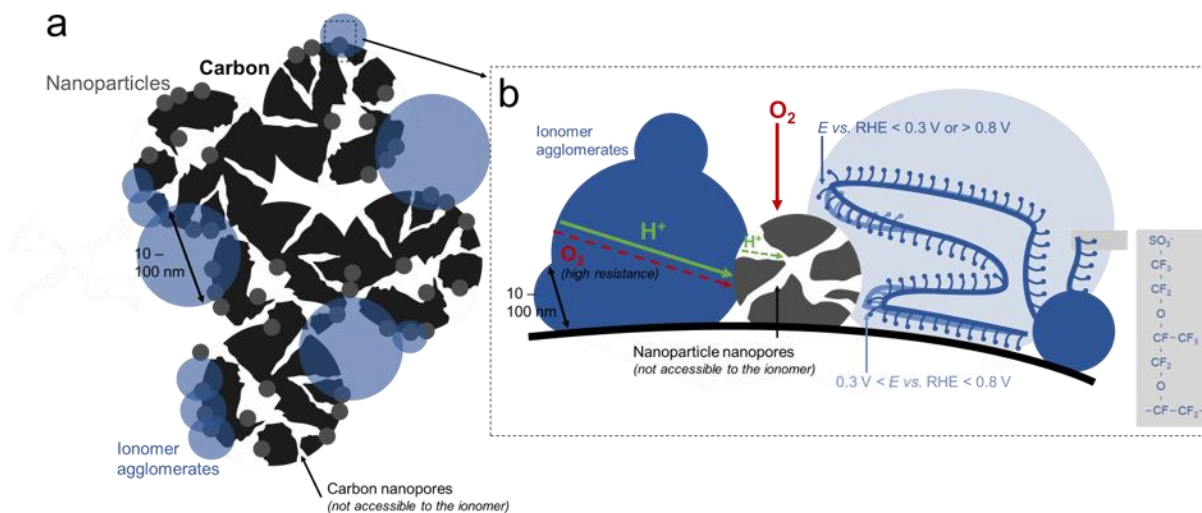
Fig 3.3 - Design challenges for Pt implementation in membrane electrode assembly; (a) schematic representation of a carbon cluster with an heterogenous coverage of the electrocatalyst surface in ionomer agglomerates and nanoparticles, along with a network of nanopores that cannot be accessed by the ionomer; (b) close-up on a single, porous, nanoparticles, with an emphasis on the non-monotonic electrostatic interactions between the ionomer and the nanoparticles.

3.3 The Shift from Liquid to Solid Electrolyte

The liquid electrolyte, *e.g.* 0.1 M $HClO_4$ or 0.5 M H_2SO_4 has high ionic strength, high proton conductivity, and allows for the electrolyte to easily penetrate the smallest porosities. In an MEA, a solid polymer electrolyte (usually, Nafion®) is used as the ion conductor and current densities are several decades higher than in liquid electrolyte (specifically with a rotating disk electrode or RDE) as a result of the small working electrode surface and the O_2 diffusion limitations observed in the 0.6 V < *E vs.* RHE < 0.8 V range [84]. Thus, the reactive interface is vastly modified when switching from liquid to solid electrolyte. In the second case, protons are transported to the electrocatalyst through (i) the ionomer network and then (ii) ionomer agglomerates around the Pt/C clusters. As illustrated in **Figure 3**, the ionomer surface coverage of Pt/C agglomerates is heterogenous [85], where some portions of carbon and Pt are

ionomer-free enabling effective oxygen transport but hindering proton transport as it results in non-ionically-connected nanoparticles (see **Figure 3a**) [86]. By opposition, large Nafion® agglomerates might cover other portions of the carbon and limiting the O_2 transport: although the exact organization of Nafion® in the catalyst layer has yet to be fully determined. It has been shown by Uchida *et al.* [87] and, more recently, Ngo *et al.* [88,89] that when Nafion® resin is dissolved in an IPA:H_2O solution, it forms aggregates of $d = 10 - 100$ nm, as illustrated in **Figure 3.** Therefore, by the size-exclusion principle, Nafion® cannot enter nanopores that are smaller than the aggregates [90] and the *close-to-ideal* concave sites constituting the inner porosities walls [44] of complex Pt-based nanostructures may be proton-limited, especially in a hot-dry condition, resulting in a drastic diminution of the performance from RDE to MEA (see **Figure 2**). Indeed, as for the carbon nanopores (where nanoparticles are also found, see **Figure 3a**), the proton transport occurring is only insured by the water produced during the ORR [91,92] or through proton surface diffusion on the carbon/platinum. Both modes of transport processes, however, present greatly increased resistances when compared to the H^+ transport in the ionomer network [93].The nanopores will also be preferentially flooded during MEA operation, enhancing proton conductivity but reducing oxygen transport (thus having similar limitations to actives sites in microporosities, *i.e.* the pores < 2 nm, see. Yang et *al.* [94]). The ionomer also poisons the Pt surface [95] as well as introducing oxygen transport resistance [96,97], especially when considering the vastly increased current densities of solid *vs.* liquid electrolyte. O_2 transports occurs under gaseous phase, through the pores of the carbon/ionomer network. However, it often has to diffuse through the ionomer agglomerates to reach the actives sites with a cost of an increased transport resistance (as evidenced by Schuler *et al.* [98] via H_2 limiting current measurments). It is also important to note that the larger size of the nanostructures

likely induces stronger electrostatic interactions with the ionomer negatively charged groups (SO_3^-) when compared to smaller Pt NPs. Platinum presents a non-monotonic charge, due to its potential of zero charge reversal at higher potential *i.e.* being negatively charged at E *vs.* RHE < 0.3 V, positively charged for 0.3 V < E *vs.* RHE < 0.6 – 0.8 V, and negatively charged for *E vs.* RHE > 0.6 – 0.8 V. Thus, for 0.3 V < E *vs.* RHE < 0.6 – 0.8 V, the Pt – SO_3^- (from the ionomer) interaction is attractive, whereas for E *vs.* RHE < 0.3 V or > 0.6 – 0.8 V, the interaction is repulsive (see **Figure 3b**) [91,92,99,100]. Attractive interactions are desirable, as protons reaches the active sites more easily, although it may result in the ionomer poisoning the Pt surface [95]. A repulsive interaction would result in a dense ionomer backbone close to the catalyst, thus resulting in higher O_2 transport resistance [96]. Increasing the NPs size results in an increased concentration of Pt charges at a given location on the carbon surface (*vs.* smaller Pt NPs), thus increasing the attractive/repulsive interactions intensity. The variety of the platinum charge and the resulting Nafion® side-chain repulsion could explain the losses in activity of some complex, yet non-porous, electrocatalysts in MEAs, such as the PtNi octahedra.

3.4 The Ideal Catalyst Layer

Several steps are to be completed in order to address the issues observed at the catalytic layer scale and at the nanoparticle scale:
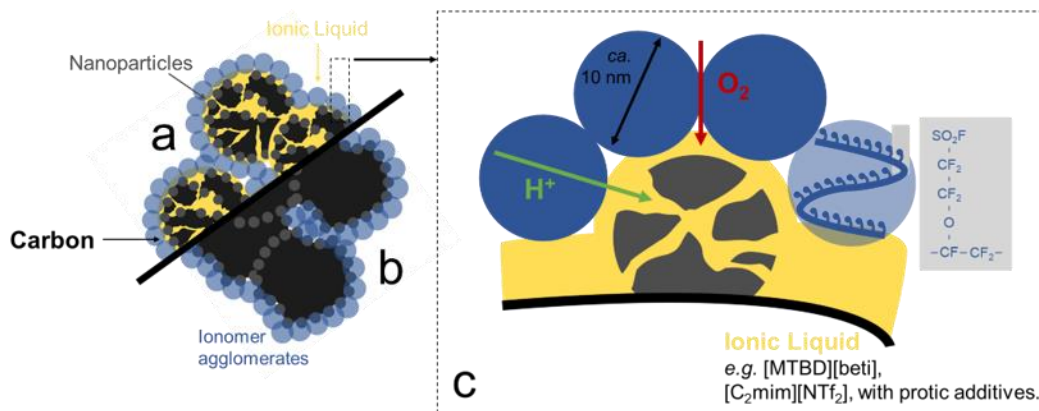
Fig 3.4 - Improving the current catalytic layer morphology; schematic representation of (a) an ideal catalytic layer achieved through the use of ionic liquid and decreased size ionomer agglomerates; (b) an ideal catalytic layer achieved by decreasing the micropores content and the ionomer agglomerates size; (c) close-up on a single nanoparticle encapsulated by ionic liquid (independently of case (a) or (b)), and with an example of a shorter chain ionomer, i.e. Aquivion®.

1. *Modifying the ink formulation.*

It has been evidenced by Van Cleve *et al.* [101] that the water to isopropyl alcohol ratio used in the catalytic layer ink preparation has a dramatic effect on the Nafion® agglomerate size. Higher water content (> 60 wt. %) resulted in smaller agglomerates but strengthen the adsorption of the SO_3^- onto the Pt surface, as a result of changes in the ionomer orientation. This confirms Ngo *et al.* [88,89], findings, *i.e.* that the presence of isopropyl alcohol is responsible for the agglomerates formation. It is notable that the activity depreciation induced by Pt/ionomer interfacial resistance as a result of the SO_3^- adsorption is lower than the improvements due to the ionomer agglomerate size decrease, with an optimum water content of 62 wt. %. Although this ratio is already the one commonly used in catalytic layers preparations, it highlights the fact that the ink preparation, independently of the ionomer, should not be overlooked. The nature of the ionomer itself can also be modified, as suggested by Garsany *et al.* [102] and presented in **Figure 4c**, as the use of Aquivion® (see

Figure 4c for the structure) *vs.* Nafion® (see **Figure 3b** for the structure) resulted in improved catalytic performances at a PEMFC cathode. Orfanidi *et al.* [103] recently shows that other ratios, such as the ionomer to carbon ratio, should also be carefully considered when preparing the electrocatalyst ink: by decreasing this ratio from 0.65 to 0.45, they successfully increased the voltage at 2 $A.cm_{geo}^{-2}$ by 20 mV. Here, it is important to note that this modification was done concomitantly to another improvement, namely the functionalization of the carbon support by NH_x groups, bringing us to a second means of addressing the issues discussed in the previous sections.

2. Modifying the support chemistry.

As stated above, functionalizing the carbon support with NH_x groups leads to a better dispersion of the Nafion® on the electrocatalyst surface, due to the coulombic interactions between the SO_3^- groups and the NH_x. Along with the improvements of the Nafion® aggregates dispersion and size, the nanoparticles dispersion should also be considered. Nanostructures tend to anchor onto the carbon structural defects and functionalities. However, a highly functionalized/defective carbon exhibits low stability in a PEMFCs cathode environment, especially during start-up and shut-down protocols as the carbon structural defects are preferentially corroded [104]. Hence, the number of anchoring sites should be increased while decreasing/maintaining the carbon defectivity. This can be achieved by doping the carbon structure with nitrogen functionalities [105], which act as additional anchoring sites without decreasing the electrocatalyst stability.

37

3. Modifying the porous network.

To address one of the most critical challenges related to the implementation of complex nanostructures supported on carbon in fuel cells, namely the small diameter of their inner porosities, a logical approach would be to design advanced nanostructures and carbon supports without nanopores (see **Figure 3a**). As suggested by Watanabe and Tryk [106] and illustrated in **Figure 4b**, the ideal catalytic layer support should present a nanopore-free structure, with nanoparticles dispersed on its surface. This aims toward the use of low specific surface, graphitized carbons that additionally present an enhanced durability. When addressing the NPs, it would suggest favoring non-porous nanostructures, such as the PtNi octahedra [42], over porous-hollow nanoparticles [49], sponges [78], or nanoframes [47]. One drawback of this method would be the low specific surface induced by the graphitic, non-nanoporous carbon support, limiting the loading of active materials on the support surface, along with the nanostructure dispersion. Hence, to maintain the advantages brought by the presence of nanoporosities, a separate approach can be considered.

4. Impregnating the porous network with ionic liquids.

Ionic liquid (IL), such as [MTBD][beti], impregnation of nanostructures and catalytic layer was investigated by Chen *et al.* [47], Snyder *et al.* [107], Benn *et al.* [108], Huang *et al.* [109] and others. Impregnated nanostructures, as the ones illustrated in **Figure 4a** and **4c**, exhibit increased performances in liquid electrolyte *vs.* the non-impregnated nanostructures. This is believed to results from the formation of a protective layer that prevents non-reactive

species adsorption on platinum [109] (hinting toward a decrease of the Nafion® - Pt interactions in presence of ILs) along with facilitating proton diffusion in the nanopore network of the carbon or active material. It is notable that ionic liquids requires the presence of a protic additive to switch from the one electron, reversible reaction $O_2 + e^- \rightarrow O_2^{\circ-}$ to the irreversible $4e^-$ reaction $O_2 + 4H^+ + 4e^- \rightarrow 2H_2O$ [110–112]. The ILs should present the following properties, *i.e.* (i) small cation/anion (to enter the nanostructure's inner porosities); (ii) good ionic conductivity; (iii) good O_2 solubility and O_2 diffusion rate; (iv) hydrophobicity. Some of these properties are difficult to achieve simultaneously, *e.g.* hydrophobicity and small cation/anion as the hydrophobicity in ILs arises from long alkyls chains, increasing the overall IL size. Additionally, IL encapsulation greatly diminishes the surface accessibility by gaseous O_2, thus explaining why a good O_2 diffusion rate/solubility is critical (see **Figure 4c**). Such properties are exhibited by some ILs, such as $[P_{66614}][NTf_2]$, $[P_{66614}]TPTP$, $[C_2mim][NTf_2]$, presenting interesting combinations of oxygen diffusion coefficient (*ca.* $7 – 10$ cm^2 s^{-1}) and oxygen solubility (*ca.* $4 – 10$ mol cm^{-3}) [110]. Using ILs would allow the protons to diffuse to active sites unconnected to the ionomer network, *i.e.* NPs inside the carbon nanopores (see **Figure 4a**) or Pt atoms inside a porous NP (see **Figure 4c**). However, there has been little to no investigation of such IL-encapsulated nanostructure performances in MEAs, and special attention should be afforded to the behavior of the H_2O generated in the nanopores during the ORR and how it may interact with the ILs in order to fully assess the viability of this method.

3.5 Conclusions

Here, we discussed the different pathways undergone to increase the activity of the platinum-based electrocatalysts, *i.e. order vs. disorder*-based approaches. Through *strain-*

ligand effect, preferential crystallite orientation, or positive use of structural defects, improvement factors of 20 – 60 compared to classic Pt NPs were achieved in liquid electrolyte. However, those improvement factors did not transpose to solid electrolyte systems (*e.g.* MEAs, PEMFCs), hence greatly decreasing their current interest. This phenomena arises from several issues, relating to the morphological properties of the improved, complex Pt-based nanostructures along with the geometry of the catalytic layer itself. These issues include (i) the nanoporosities in the carbon support and the nanoparticles, inaccessible by Nafion®, which are easily flooded and contain active sites that have little to no contribution to the overall catalytic activity; (ii) an increased size of nanoparticles leading to an increased electrostatic interaction with the Nafion® backbone; (iii) a heterogeneous dispersion of nanoparticles onto the carbon support structure. To overcome these challenges, several options can be explored, *i.e.* encapsulating the NPs and filling the nanopores with ionic liquids that have defined properties (low cation/anion size, high ionic conductivity, oxygen solubility and oxygen diffusion coefficient, *etc*.); favoring nanopore-free nanoparticles and carbon support materials; functionalizing the carbon surface with nitrogen or NH_x groups, thereby increasing the anchoring site density, facilitating the nanoparticle dispersion, and decreasing the Nafion® agglomeration. Lastly, the ink preparation process as well as the ratio between the water, alcohol, carbon, and ionomer must be optimized.

4. Platinum Nanoflowers as a Cathode Catalyst in PEMFCs

Here, we investigate the oxygen reduction reaction activity of near-monocrystalline platinum nanoflowers presenting a low microstrain to decorrelate the contribution of (i) distorted lattice and (ii) high coordination active sites found within the Pt nanoflowers porosities (*i.e.* with an optimal generalized coordination number for OH_{ads} binding) to the specific activity enhancement. The results are discussed in the frame of previous investigations onto various catalytic nanostructures. We evidenced that the microstrain of the platinum nanoflowers stand out of the trends previously established for defective Pt-based nanostructures onto which the activity is driven by lattice distortion. This indicates that (i) 'defective' structures with low lattice distortion, but high variation in coordination number, can be synthesized and (ii) that their activity improvement is comparable to the surface distortion approach in liquid electrolyte. However, their implementation in proton exchange membrane fuel cells remain challenging, as a substantial drop in performances is observed when switching from liquid to solid electrolyte, due to (i) the low specific surface of the nanoflowers and (ii) the higher high frequency resistance exhibited by the latter.

4.1 Introduction

Platinum (Pt) is the leading electrocatalyst for use in hydrogen-based polymer electrolyte membrane fuel cells (PEMFCs) for the sluggish, cathodic oxygen reduction reaction (ORR).[3,4,9,113–116] The scarcity and high price of platinum remain as a major roadblock and even state-of-the-art Pt-based catalysts still lack the activity and stability needed for wide-scale commercial deployment.[5,117] To overcome these issues, the recent development of Pt-based catalysts has turned away from the traditionally small, spherical nanoparticles of Pt to advanced structured nanoparticles in order to improve the intrinsic activity, electrochemically active surface area (ECSA), and stability during operation.[19,118,119] Starting from the work of

Stamenkovic *et al.* that underlined the substantially increased activity of $Pt_3Ni(111)$ crystal facets and the works from Strasser's group that evidenced the superior performances of Pt_xNi octahedral nanoparticles (*i.e.* dominated by (111) facets) for the oxygen reduction reaction, [120–124] new directions have been undertaken to improve Pt-based electrocatalysts activity. Firstly, it was evidenced that the addition of alloying elements to the platinum crystal structure led to higher activities due to the strain effect, *i.e.* the contraction of the surface lattice parameters by sub-surface 3d-transition metals.[20,121,125,126] Highly porous structures are also of interest due to their high surface area to volume ratio in comparison to its similarly sized solid counterpart, thus significantly increasing the active site density (and ECSA) as well as reducing the amount of precious metal required.[127–129] Finally, structural disorder (*i.e.* variations in the local coordination and lattice parameter) has been shown to greatly influence the ORR performance of Pt-based nanostructures.[119,130,131] In the light of the recent progresses in electrocatalyst design, two approaches seem to exist, *i.e.* disorder based, which consist in increasing the structural defects density to an optimum and order-based, which evolve around finely tuning the structure to expose the facets with the highest activity, and transition elements density in the sub-surface layers. Within the disorder-based approaches, it can be argued that the contribution of structural defects arises from two different aspects (i) the variation of the local coordination induced by the presence of crevasses or ad-atoms leading to either over, under or adequately coordinated (generalized coordination number below, above or equal to 8.3, respectively [132]) and (ii) the variation of the local lattice parameters, evidenced by the presence of microstrain, lead to either over, under or adequately packed atoms.[133] Decorrelating those two contributions is challenging, as structurally disordered electrocatalysts often present both high local variations in the coordination number (*i.e.* high density of crevasses, pores, adatoms)

and highly polycrystalline structures that result in important microstrain. The objective of this work is thus to design a nanostructure exhibiting only one kind of structural defect, *i.e.* high variation of the local coordination number (*e.g.* due to porosities) without microstrain (*i.e.* a near monocrystalline structure, without alloying elements) to be compared, performance-wise and physicochemical-wise, with a well-defined and understood defective nanostructure, the platinum-based 'sea-sponges'. The paper will first discuss the synthetic pathway undergone to achieve said nanostructure, along with the innovative approach taken to remove active-site-poisoning organics tightly adsorbed or bound to the surface,[134–136] before addressing its ORR activity and how it fits within the family of the disordered nanostructures, to finally discuss the implementation of such complex nanostructures in proton exchange membrane fuel cells.
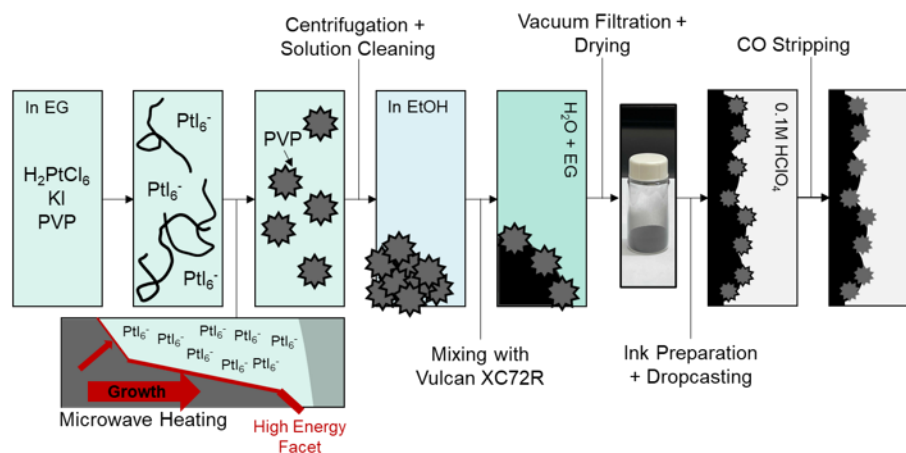
Fig 4.1 - Synthesis pathway undergone for the preparation, and cleaning, of the platinum nanoflowers.

4.2 Nanoflower Synthesis

Hollow and porous nanoparticles have typically been prepared through subtractive growth or etch mechanisms, which tends to produce higher concentrations of microstrain-based

43

structural defects (*e.g.* presence of an alloying element).[128] Here, platinum nanoflowers are synthesized with an adapted polyol method with a suspected additive growth mechanism (**Fig 1**).[22,137–140] This facile, one-pot synthesis produces a high yield of similar nanostructures with no additional materials synthesis treatments required. The modified polyol synthesis procedure utilizes a platinum salt precursor, iodide ions (for structure formation), and a polymeric surfactant all dispersed in ethylene glycol with microwave-assisted heating.[141–144] Our understanding of the formation mechanism is that the chloride ion complex ($PtCl_6^-$) shifts in solution to an iodide ion complex (PtI_6^-) with the addition of iodine ions, as indicated by the immediate shift in solution color (yellow → orange → red). Studies of branched Pt nanoparticles have assessed that, if the growth kinetics dominates over the surface diffusion rates, anisotropic growth and anisotropic nanostructures are to be observed as final products.[145] The more stable iodine complex leads to a higher instantaneous concentration of Pt-based species in solution inducing a easier replenishing of the Pt precursors at the existing Pt seed interface, which thus favor growth kinetics limitation and thus, the growth of higher energy facets.[137]
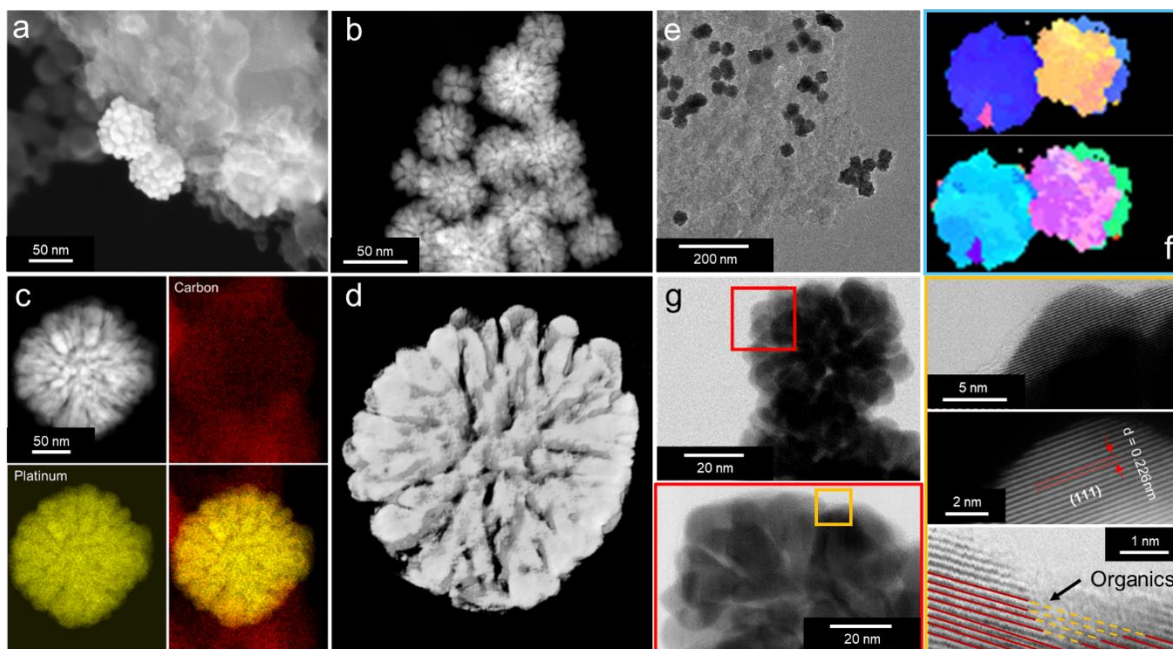
Fig 4.2 - Micrographs of the platinum nanoflowers (d = 40 – 45 nm) obtained by (a) scanning electron microscopy, (b) high annular angle dark field scanning transmission electron microscopy on unsupported nanostructures, (c) energy dispersive X-ray elemental mapping; (d) electron tomography (see supporting information for the different angles); (e) dispersion of the platinum nanoflowers onto Vulcan XC72R, (f) orientation mapping of the platinum nanoflowers and (f) high resolution micrographs aiming to provide insights onto (i) the monocrystallinity of the Pt nanoflowers and (ii) the organic presence prior to the CO cleaning step.

4.3 Nanoflower Structure Analysis

Transmission electron microscopy (TEM) images show platinum nanoflowers centered around 40 - 45 nm and good spatial dispersion on the Vulcan XC72R, as illustrated on **Fig. 2**. High-resolution scanning transmission electron microscopy (HR-STEM) images show that the Pt nanoflowers are coated with a 1-2 nm thick layer of organics as well as displaying a continuous crystallinity that is unbroken across pore channels (**Fig. 2g**). The crystallite size for these nanoflowers was determined, from the XRD patterns (**Fig. 3**) to be *ca.* 20 nm which suggest that the structure has a minimal amount of grain boundaries compared to an analogous nanostructure, the "sea-sponge" type Pt-based electrocatalyst.[130] This is further confirmed by

(i) the orientation mappings (**Fig. 2f**) that evidenced that the nanoflowers are often mono- or bi-crystalline and (ii) the wide angle X-ray scattering performed at the ID-31 beamline (ESRF), which evidenced a coherent domain size of *ca.* 17.5 nm, thus resulting in a microstrain of 24 %% and a surface distortion of 3.1 % (see Chattot *et al.* for the calculation of the surface distortion, *i.e.* the density of microstrain-related structural defects assuming that the latter **only** originate from the crystallites surface). For comparison, the "sea-sponges" exhibit a *ca.* 230 %% microstrain and, as a result, a *ca.* 8 % surface distortion for a crystallite size of *ca.* 9 nm. Finally, X-ray absorption spectroscopy was performed at the Advanced Photon Source with the XANES and EXAFS data confirming that the nanoflowers behave as bulk Pt, further confirming the nanostructure monocrystallinity (**Fig. 3b-c**).[146] Electron tomography of a single nanoflower was completed by a HR-STEM tilt series (± 20°) and the resulting bright field images were stacked and aligned to create a 3D motion picture of the nanoflower (**Fig. 2d** and supporting information). We reconstructed the tomogram using the overlapping data from the tilt series showing the complexity of the inner pore structure which is continuous from the center of the particle to its surface (**Fig. 2**).
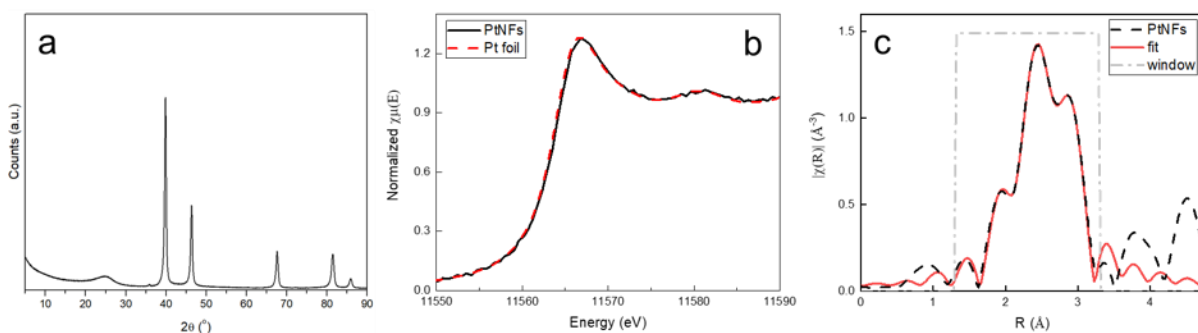
Fig 4.3 - X-ray properties of the platinum nanoflowers (a) X-ray diffraction pattern of the nanoflowers supported onto Vulcan XC72R (b) X-ray absorption near the edge structure and (c) extended X-ray absorption fine structure for the platinum nanoflowers supported on Vulcan XC72R vs. Pt foil.

4.4 Carbon Monoxide Surface Cleaning Protocol

One of the major issues for the deployment of advanced structured nanoparticles is the remaining adsorbed organics originating from the synthesis process. In this case, polyvinylpyrrolidone (PVP), used as a surfactant, tends to be strongly absorbed or bound to the surface of the Pt nanoflowers and is apparent in HR-STEM (**Fig. 2g**) and pre-treated electrochemical tests.[135] Bulky organics used in the synthesis stage are typically removed by either solvent cleaning cycles or heat treatments, however the pore structure of the nanoflowers disallows both methods of removing leftover organics: (i) multiple solution-based cleaning protocols were tested to remove organics, however this type of cleaning had little effect; (ii) high temperature heat treatments (~300-600°C) in inert atmospheres and under vacuum were investigated, however those methods caused significant morphological degradation and complete pore structure collapse of the nanoflowers.[147–149] So, to obtain an electrochemically pristine surface, a carbon monoxide (CO) surface cleaning method was adapted from a previous work.[134], which allowed a complete removal of the organic within three experimental

47

cycles (see experimental section and **Fig. 4**). Interestingly, the CO cleaning protocol shows a high potential peak in the first stripping cyclic voltammetry, followed by a much lower potential peak in successive strippings, suggesting that the CO_{ads} binding strength is greatly affected by the PVP presence. This could either arise from (i) the PVP-induced steric encumberment of the platinum surface, which limits accessibility to the OH_{ads} species or (ii) PVP-induced modification of the platinum electronic structure, which either strengthen the CO_{ads} adsorption or weaken the OH_{ads} adsorption.[130,131]. Notably, the mono-peak signal of the platinum nanoflowers provide further evidence of the near-monocrystallinity of these structures, as Maillard *et al*. evidenced that the presence of grain boundaries was concomitant with the apparition of a pre-peak in the CO_{ads} stripping signal.[150]
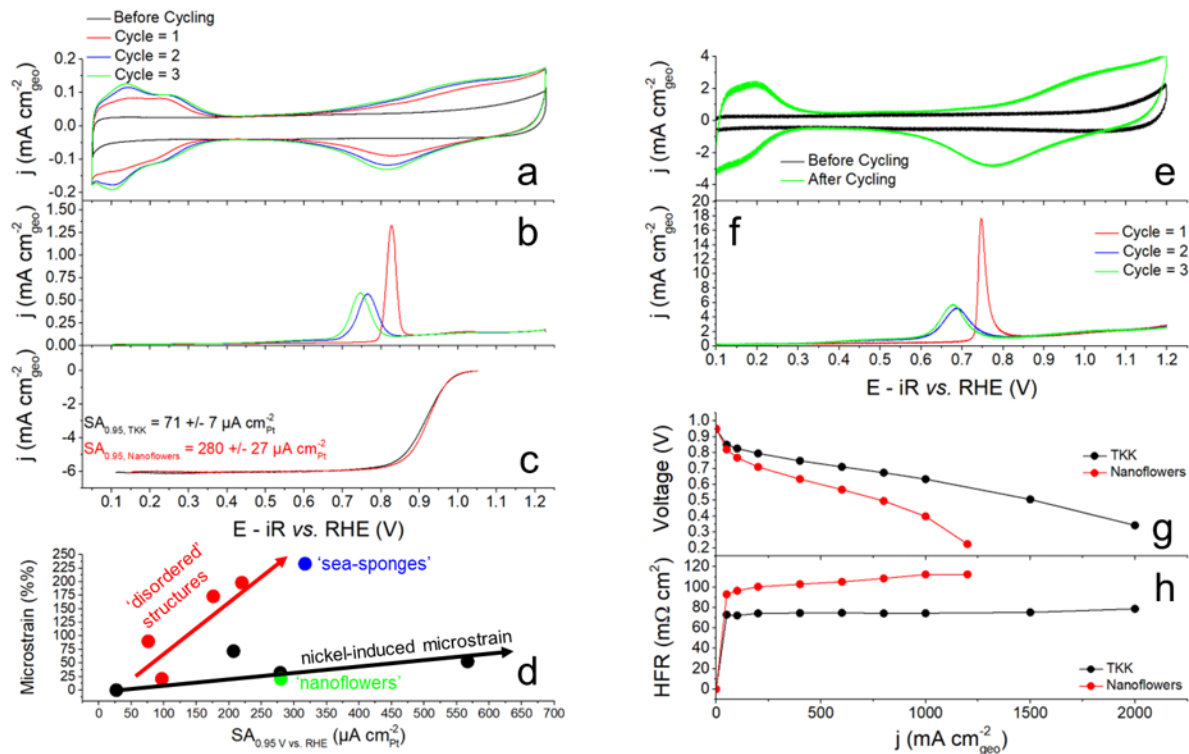
Fig 4.4 - Electrochemical properties of the platinum nanoflowers supported on Vulcan XC72R and comparison with the literature: (a) cyclic voltammetry in N_2-saturated 0.1 M $HClO_4$ (20 mV s^{-1}), before and after CO_{ads} cleaning; (b) CO_{ads} stripping cycles leading to the surface cleaning; (c) linear sweep voltammetry in O_2-saturated 0.1 M $HClO_4$ (20 mV s^{-1}, 1600 r.p.m) for Pt/C provided by TKK and the platinum nanoflowers; (d) microstrain as a function of the specific activity at E vs. RHE = 0.95 V ($SA_{0.95\ V\ vs.\ RHE}$) for the nanoflowers and the library of electrocatalysts investigated by Chattot et al., i.e. 'ordered' structures, that exhibit only Ni-induced microstrain; 'disordered' structure where the defective nature is dominated by local variation of the lattice parameter, which include the PtNi sea-sponges; (a) cyclic voltammetry during MEA characterization, under N_2-atmosphere, before and after CO_{ads} cleaning; (b) CO_{ads} stripping cycles in MEA leading to the surface cleaning; (g – h) polarization curves measured under air, with a backpressure of 150 kPa and 100% relative humidity, for the Pt nanoflowers and the Pt/C TKK reference, along with the variations of the high frequency resistance (HFR) as a function of the applied current.

4.5 Oxygen Reduction Reaction Performance

The nanoflowers were studied in 0.1 M $HClO_4$. It was found that, like most advanced structure catalysts, they suffered from a significant loss in ECSA compared to traditional nanoparticles, i.e. 18 m^2 g_{Pt}^{-1} (calculated from the H_{upd}) or 13 m^2 g_{Pt}^{-1} (calculated from the

49

CO$_{ads}$ stripping) *vs.* 90 m^2 g$_{Pt}^{-1}$. However, the nanoflowers specific activities 4-fold higher compared to industry standard Pt/C catalysts (see **Figure 4c**), thus implying that some of the nanoflowers active sites exhibit far higher intrinsic activity than the Pt/C active sites. Owing to the fact that the nanoflowers do not present clearly defined facets, by opposition to nanostructures such as Pt$_x$Ni octahedra, this intrinsic activity enhancement is likely to arise from structural defects and, more specifically, (i) surface lattice distortion or (ii) variations in the local coordination number. Identifying which of those two predominates can be done by comparing these structures by those discussed by Chattot *et al.* [130,131]. Here, we aim to assess if the microstrain and the surface distortion of the Pt-nanoflowers follow the same trend as the one observed for nanostructures for which the intrinsic activity results from high lattice distortion. This trend is presented in **Figure 4d**. The nanoflowers present an extremely low microstrain (21%%), which bring them within the family of catalysts where the microstrain solely results from the presence of an alloying element – which, incidentally, is absent from the Pt nanoflowers. This further strengthen the hypothesis that the nanoflowers only present little structural defects and that the activity arise from the high coordination active sites present within their porous networks. One could argue that not the microstrain, but the surface distortion, should be used as a comparison vector here but (i) the surface distortion model was developed for 2 – 5 nm, cubooctahedral crystallites, which are extremely different to the crystallites morphology within the nanoflowers, thus rendering the use of such model extremely challenging; (ii) by considering the surface distortion and thus only acknowledging the crystallites surface contribution lead to a surface distortion value of 3.1%, which is far below the values observed for structures of similar activities for which the activity enhancement was mainly induced by the local variation of the lattice parameter. In essence, it

appears from the comparison with previous works that the platinum nanoflowers do not follow the trend commonly observed for defective nanostructures. As such, their activity improvement is neither correlated to surface distortion or strain, ligand, or specific orientation effects, but to local variations of the generalized coordination number. Keeping in mind the final application of the platinum nanoflowers, the latter were characterized as the cathodes of membrane electrode assemblies (MEA), leading to several critical findings: (i) the CO_{ads} stripping cleaning method successfully operates in solid electrolyte environment, as evidenced in **Figure 4e-f**; (ii) the performances of the platinum nanoflowers under air-atmosphere were lower than those observed for the Pt/C TKK standard (**Fig. 4g**). Specifically, although the onset potentials are identical, the platinum nanoflowers show slower increase in current density with the voltage decrease, that primarily arise from an higher high frequency resistance (HFR, see **Fig. 4h**), indicating that the nanoflowers limitations are induced by an high proton resistivity within the cathodic catalytic layer, symptomatic of a poor impregnation of the nanoflowers by the ionomers, due to (a) size exclusion induced by the presence of the organics that were originally blocking said porosities and/or (b) the small radii of the latter which limits the ionomer penetration.

4.6 Conclusions

In summary, we successfully synthesized platinum nanoflowers that intrinsic activity is mainly driven by active sites with near-ideal coordination, as they exhibited little microstrain, along with the absence of (i) alloying elements and (ii) extended facets. As such, those nanostructures present an interesting counterpart to the 'surface distortion' based nanostructures, evidencing that similar intrinsic activity can be achieved through the use of different kinds of structural defects. However, those materials exhibit strong limitations for

their implementation in solid electrolyte, that are mainly induced by the higher HFR presented by the nanoflowers catalytic layer, which results of poor integration of the ionomer within the nanostructures inner porous network.

5. Incorporating Metal-Nitrogen-Carbon Materials in PEMFCs

Here, we investigate the electrocatalytic oxygen reduction and carbon monoxide oxidation reaction improvements through the usage of combined metal-nitrogen-carbon catalysts and platinum-based catalysts. The created library of metal-nitrogen-carbon materials showed strong trends of activity and reaction energy shifts when decorated with the traditional platinum nanoparticle catalysts. The results align with previous works and show that despite the small metal weight loadings of metal-nitrogen-carbon materials (~1-2 wt. %) and the significant size differences (i.e., 2-3 nm Pt nanoparticles vs. single-atom metal sites), that the interactions between the atomically dispersed metal sites and the nanoparticles can substantially influence the molecular binding and catalytic properties of the active sites. These interactions could theoretically be tailored using multi-metallic blends of metal-nitrogen-carbon materials to improve both the activity and the stability of the platinum-based catalyst.

5.1 Introduction

Platinum has traditionally been the catalyst material of choice for the sluggish oxygen reduction reaction (ORR), which is the limiting factor of the hydrogen-based polymer electrolyte membrane fuel cell (PEMFC). However, in recent years, the development of the precious-metal-free (or platinum-group-metal-free, PGM-free) catalysts, typically metal-nitrogen-carbon based materials, has been able to catch up to the vicinity of platinum's intrinsic activity. And while efforts to reduce the amount of platinum used or improve platinum's activity have made leaps and bounds in the field, the high prices and scarcity of the metal has

still been a major roadblock for the deployment of the wide-spread commercial use of PEMFCs.[9,113,117] On the other hand, the rapid improvements of metal-nitrogen-carbon materials have begun to reach a plateau and still has major roadblocks of activity and durability issues that must be improved prior to its commercial deployment.[5,151,152] The combination of both catalyst types (platinum-based and metal-nitrogen-carbon) has been explored only recently with works looking into the utilization of platinum nanoparticle ultra-low and normal loading onto M-N-C materials. Generally, the field is split into two categories with obtaining synergistic effects: the use of platinum nanoparticles as an additive for M-N-C catalysts or the substitution of the carbon support with M-N-C materials in platinum-based catalysts.[7,8,15–18] The addition of platinum as an additive utilizes the nature of platinum to be a strong peroxide scavenger which prevents the rapid degradation of the M-N-C catalyst due to the production of caustic hydrogen peroxide through the parasitic $2e^- + 2e^-$ transfer pathway (compared with the ideal $4e^-$ transfer pathway leading only to the formation of water).[7,8] The substitution with M-N-C materials is simply to replace an inactive carbonaceous support material with a material that has an intrinsic activity for the oxygen reduction reaction in order to improve the catalyst layer performance.[15–18] However, recent works have shown that there may be further beneficial interactions (other than just the addition of the activities for the active material and active support) that occur from incorporating platinum nanoparticles with M-N-C materials.[153] From the groups of Gang Wu and Shichun Mu, it was found that the strong interactions occurred between the single-atom sites of the M-N-C support material and the platinum nanoparticles. These measured interactions suggest that the significant activity or durability improvement (depending on which single-atom element is doped into the support material) is more convoluted than just the basic addition of the activities of the platinum and M-N-C materials.

53

Additionally, groups have reported on a "ligand field effect" in which proximity dopant atoms can affect the electronic properties of the primary dopant atom.[152,154] The combination of the "ligand field effect" with the effects seen by the incorporation of M-N-C materials as Pt nanoparticle supports suggest that these effects may be tailored by a precise tuning of elemental composition of multi-doped M-N-C materials. Such materials could change the oxygen intermediates binding energy of the active Pt nanoparticles in smaller increments towards the top of the volcano trend.[155] The objective of this work is to look at the trends of a large elemental library of M-N-C materials to deconvolute the effects that the single-atom sites can have on the platinum active sites. Firstly, we look at the ORR activity trends of the bare and hybrid catalysts as well as recording the peroxide yields that occur to build a periodic table heatmap in activity improvements. Secondly, we look into the carbon monoxide oxidation behavior of the platinum in the hybrid catalysts to understand surface energetic changes that the single-atom sites can have on the platinum nanoparticles. And lastly, we test the durability of a selected group of catalysts to understand whether the activity and durability improvements have interplay (i.e., the increase of one may lead to the decrease of the other).
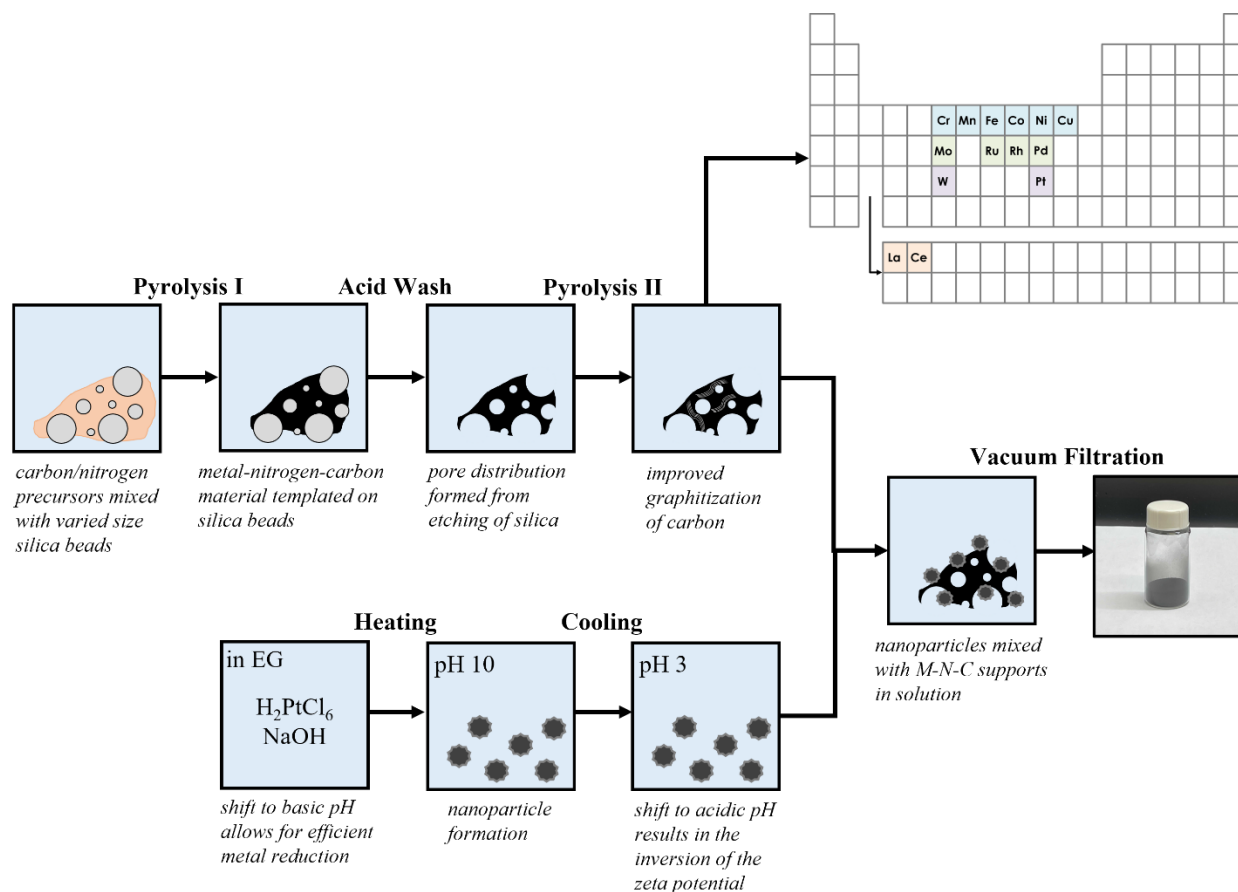
Fig 5.1 – The synthesis procedures for both the M-N-C material (with the elements used highlighted in the periodic table insert), the Pt nanoparticles, and the hybrid Pt/M-N-C catalyst.

5.2 MNC Materials and Pt Nanoparticles

M-N-C Materials

Atomically dispersed M-N-C materials were synthesized via the robust sacrificial support method (SSM), originally developed by our group. The SSM has been extensively practiced for first row transition metals and utilized for the ORR and CO_2 reduction reaction (CO_2RR). Here we extend the SSM to include 4d, 5d and f-metals and synthesized a set of 15 M-N-C catalysts (a metal-free N-C along with M = Cr, Mn, Fe, Co, Ni, Cu, Mo, Ru, Rh, Pd, La, Ce, W and Pt) as shown in Fig. 1. Synthesis parameters were optimized to maintain an atomic dispersion for each metal element (see methods section).

55

Representative AC-HAADF STEM images are shown in Fig. 2c, for Mn-N-C (3d element), Rh-N-C (4d element), and Ce-N-C (5d element) confirming the atomic dispersion of the metal sites. The XRD patterns (Fig. 3d) show only the (002) and (100) carbon peaks, further demonstrating the absence of crystalline metallic nanoparticles. The morphology of the M-N-C supports was examined through Raman spectroscopy and N_2-physisorption. The quantification of different carbon phases through Raman is shown in Fig. 3c, highlighting a similar, largely amorphous carbon structure (30-45%), with slight graphitization (15-20%) for all the M-N-C supports. Fig. 3a shows the typical pore size distribution for the SSM, with 2 peaks (*ca.* 20 nm and *ca.* 65 nm) indicating a strong mesoporosity imparted by the sacrificial silica template. Furthermore, all M-N-C materials demonstrate a consistent BET surface area as determined by N_2-physisorption. XPS was used to confirm the formation of $M-N_x$ moieties (thought to be largely responsible for the ORR activity of M-N-C catalysts), as well as other N-moieties (pyridinic, pyrrolic quaternary, and graphitic) that have been speculated to have ORR activity. Fig. 3e, shows the quantification of the N-moieties determined by deconvoluting the high-resolution N 1s spectra, confirming the formation of M-Nx moieties in all M-N-C supports. Advanced characterization of the M-N-C materials employed in this work, utilizing AC-STEM/EDS, single atom EELS, and XAS to confirm the atomic dispersion and nitrogen coordination of the $M-N_x$ sites, is given in our recent work, where this set of M-N-C catalysts was developed to evaluate the reaction pathways for the nitrate reduction reaction to ammonia.
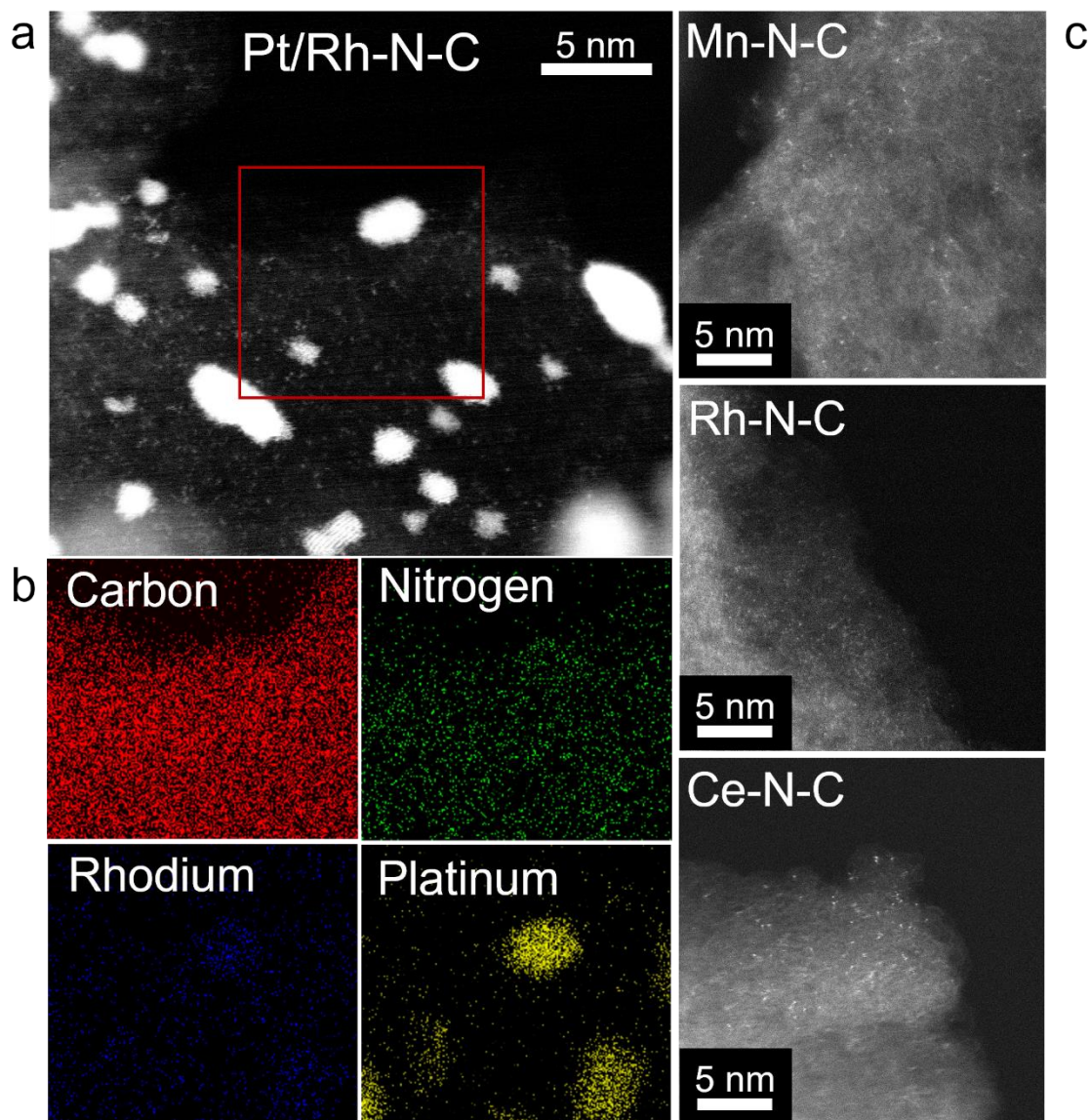
Fig 5.2 – Micrographs of (a) the hybrid Pt/Rh-N-C catalyst, (b) the EDS mapping signals of C, N, Rh, and Pt, and (c) representative bare M-N-C sample from each periodic row (3d, 4d, 5d).

Pt Nanoparticles

We synthesized a large-scale batch of Pt nanoparticles (to avoid issues of batch-to-batch variation) based on a previously reported, adapted version of the classical polyol method.[139,140] These nanoparticles have an average size of ~2-3 nm in diameter with a uniform size distribution and active surfaces that are easily cleaned via electrochemical

potential cycling as large surfactants are not used in this synthetic method (Fig. 1). The nanoparticles were made separately from and then decorated onto the M-N-C materials at ambient conditions, preventing the alteration of the M-N-C material during the creation of the hybrid catalyst. It was found that the platinum nanoparticles dispersed evenly onto the M-N-C materials and no platinum nanoparticle agglomeration or metal (from the M-N-C material) clusters or nanoparticles were detected by STEM and XRD (Fig. 2 and 3).
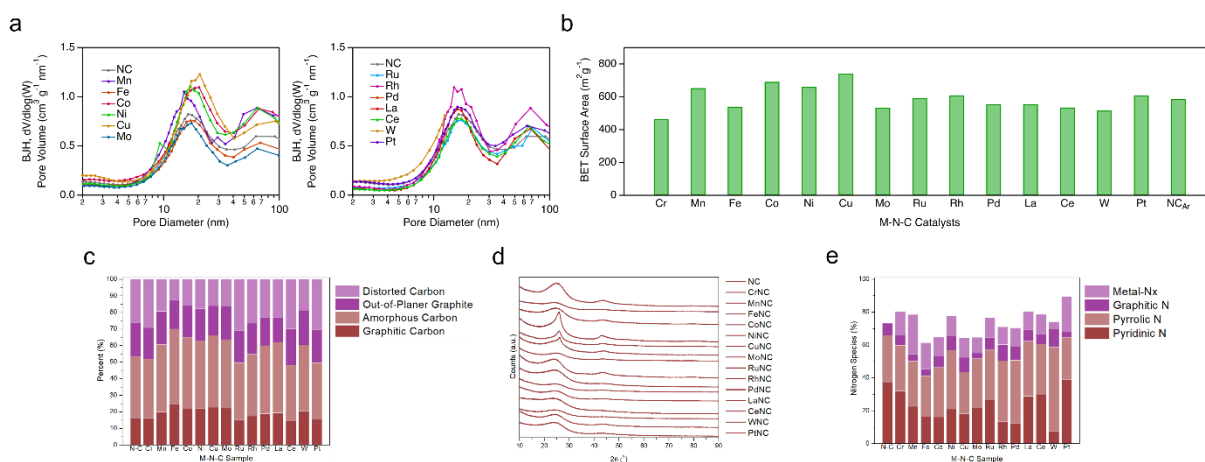
Fig 5.3 – (a) Pore size distribution, (b) Brunauer-Emmett-Teller surface area, (c) carbon-type content (from Raman spectroscopy), (d) X-ray diffraction patterns of the bare M-N-C materials, and (e) N-species breakdown of total N-content.

5.3 Bare MNC Materials Performance

The M-N-C materials were first tested as singular catalysts to build an experimental volcano trend of their activity and to understand the baseline activity of the available active sites, which are believed to be the $M-N_4$ sites as deduced by previous works (Fig. 3 and 4).[5,156–158] Our experimental results showed parabolic activity trends occurring throughout each periodic row (i.e., 3d, 4d, and 5d transition metal doped M-N-C materials) resulting in a local periodic table activity maximum with Fe-N-C and Rh-N-C materials (Fig. 4). Our elemental

trends agree with previous elemental library works on the dopant effect of M-N-C materials on ORR activity.[159] To confirm that the metallic active site dominates in the performance of bare M-N-C materials, a metal free N-C material was used as the baseline of the activity and, indeed, we find that the metal-free N-C catalyst has the lowest performance of the catalyst library.
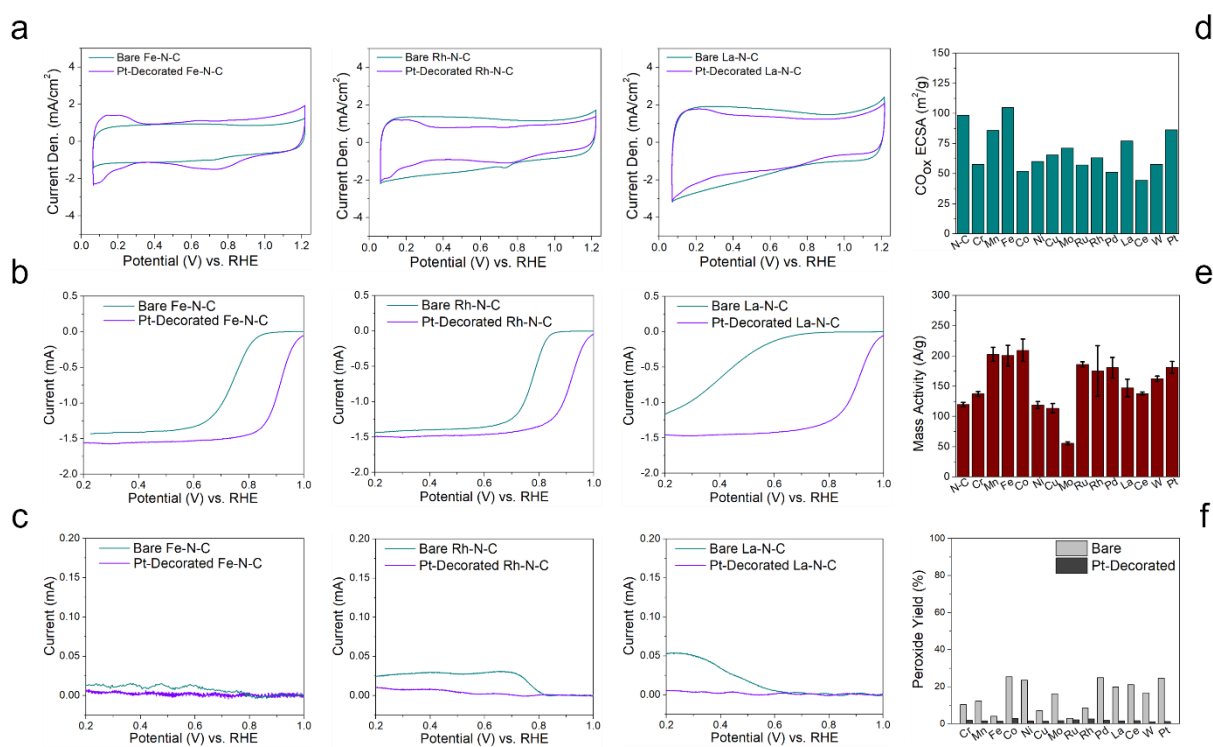
Fig 5.4 – (a) Cyclic voltammograms (taken at 20 mV/s), (b) ORR linear sweep voltammograms (taken at 5 mV/s), and (c) ring linear sweep voltammograms (taken at 5 mV/s) of bare M-N-C and hybrid Pt/M-N-C catalysts. (d) Pt electrochemically active surface area, (e) Pt mass activity, and (f) peroxide yield percentages of hybrid Pt/M-N-C catalysts.

5.4 Platinum-decorated MNC Materials Performance

The hybrid Pt/M-N-C catalysts were tested in the same fashion as the bare M-N-C materials to elucidate possible unique interactions between the platinum nanoparticles and the embedded metal atoms in the support. Our results show that the combination of platinum with the M-N-C materials leads to the activity domination with the platinum active sites and the M-N-C material providing a slight boost to the overall activity (calculated at 0.90 V) dependent on the performance of the bare M-N-C materials (i.e., higher bare catalyst performance contributes a larger boost to the overall hybrid catalyst activity) (Fig. 4). To confirm that the interactions are more than typical sample-to-sample variations, cyclic voltammetry of the hybrid catalysts was also analyzed. CV comparison of the catalyst library showed changes in peak position and peak intensity in the hydrogen and oxygen intermediates adsorption/desorption peaks (Fig. 4). Most notably, the effect of using Mo-N-C as the support catalyst for the Pt nanoparticles caused additional peaks to appear in the CV (which were not seen with bare M-N-C or typical Pt NPs) signifying a change in a molecular binding behavior of the Pt active surface.

Despite the slight sample-to-sample variation for metal weight loading (for Pt and metal dopants), there were no observable trends in the sample set for the dependency of activity or electrochemically active surface area with the metal loading amount. Although it's been shown previously that higher Pt loading samples typically perform better than lower loading samples (when normalized to total metal weight), the target loading of this work was 10-20 wt. % Pt in order to prevent total activity domination from the platinum with ultra-high loadings (>40 wt. %) and to prevent the inactivation of platinum with ultra-low loadings (<5 wt. %).[7,8]

5.5 Catalyst Peroxide Yields

Our results show widely ranging peroxide yields (up to 25%) among the bare M-N-C catalysts, however there are no clear periodic trends for the total amount of peroxide production among different transition metal dopant elements (Fig. 4). Despite recording peroxide yields ranging from 3% to 25% from the bare M-N-C catalysts, the hybrid Pt/M-N-C catalysts saw a dramatic reduction in total peroxide yield across all samples with none surpassing 3% (Fig. 4). Interestingly, the trends in peroxide yield do not match between the bare M-N-C catalysts and the hybrid Pt/M-N-C catalysts (i.e., the lowest or highest yield for bare catalysts does not always match the lowest or highest yield for hybrid catalysts). These results are aligned with previous reports of utilizing ultra-low doping of Pt nanoparticles onto M-N-C catalysts for the sequestration of the corrosive peroxide by-product.[7,8]
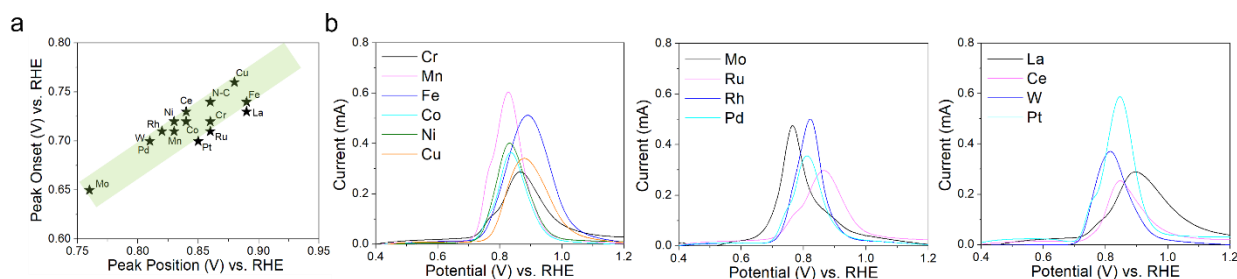
Fig 5.5 – (a) CO stripping peak onset vs. peak maximum potentials and (b) baseline-corrected CO oxidation curves.

5.6 Carbon Monoxide Oxidation

To further investigate the effects of the M-N-C material as a support towards the surface properties of the Pt nanoparticles, we tested the CO oxidation by the hybrid Pt/M-N-C catalyst library. The ORR active site on the M-N-C support is presumed to be inactive for the CO

oxidation reaction and the Pt nanoparticles are taken from the same synthetic batch, thus any shifts or shape changes in the CO oxidation peak is assumed to be due to the effect of changing the support material (i.e., the atomically dispersed metal sites influence onto the Pt active sites). From the baseline-corrected CO stripping curves, we find that samples differ in peak shape (with some samples recording two distinct peaks and others recording a singular peak) as well as peak position (onset potential and max intensity peak location) (Fig. 5). Looking at the graph of the compiled data (Max Intensity Peak Position vs. First Peak Onset), we see that the samples lie on a general linear trend (Fig. 5). This linear trend represents that the FWHM of the main CO oxidation peak of all samples is fairly similar and suggests that the mechanism of CO oxidation among all samples is the same, as expected. Therefore, the CO oxidation peak shifts must be mainly affected by the nanoparticle-support interactions from changing the M-N-C material, arising from the element change in the single atom metal sites. The CO oxidation reaction shows that the platinum catalytic surface activity can be altered by different M-N-C materials suggesting an influence of the electrostatics of the support material onto the nanoparticles and, in this case, resulted in samples shifting towards better or worse CO poisoning tolerance.
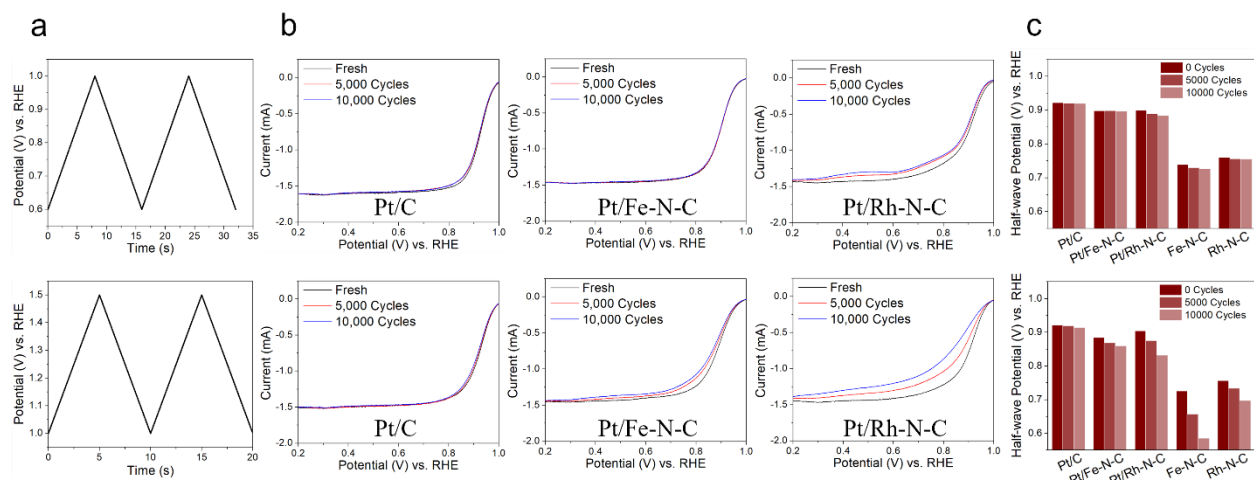
Fig 5.6 – (a) Triangular wave potential sweep patterns for the low potential (load cycling) and high potential (start-up/shut-down) regions, (b) ORR linear sweep voltammograms (taken at 5 mV/s) as a fresh sample and after 5,000 and 10,000 cycles of the Pt standard and hybrid Pt/M-N-C catalysts, (c) half-wave potentials at 0/5,000/10,000 cycles of bare and hybrid catalysts.

5.7 Catalyst Durability Under Load-Cycling and Start-Up/Shut-Down Protocols

The carbon support is known to significantly impact the catalyst durability through its materials properties (i.e., carbon porosity, surface chemistry, and graphitization) and previous works have hypothesized that the strengthened nanoparticle-support interactions as well as the strengthened ionomer-support interactions of incorporating M-N-C materials contribute to these effects.[15,16] Although the true behaviors are yet to be determined, the atomically dispersed metal sites is believed to have strong interactions with the Pt nanoparticles (possibly with anchoring and electrostatic effects) and similarly, the effect of nitrogen doping of the support is believed to aid in the anchoring of the ionomer, both of these effects may provide better ionomer coverage of the nanoparticles while possibly decreasing the nanoparticle diffusion and dissolution.[9,21,160] To elucidate these effects, we compared the degradation behaviors of 5 samples (Pt/C standard, Pt/Fe-N-C, Pt/Rh-N-C, Fe-N-C, and Rh-N-C) over two potential ranges (0.6V-1.0V vs. RHE for a drive cycle protocol and 1.0V-1.5V vs. RHE for a start-up

63

shut-down protocol) (Fig. 6).[161] In the lower potential range (0.6V-1.0V vs. RHE), which typically affects the Pt nanoparticle degradation more, we found that the Pt/FeNC and the Pt/C standard had essentially no losses while the other samples degraded only slightly after 10,000 cycles. However, in the higher potential range (1.0V-1.5V vs. RHE), which typically affects carbon corrosion degradation more, we found that all samples had significant degradation with the Pt/C standard suffering the least. Interestingly, the bare Fe-N-C catalyst suffered much more than the Pt/Fe-N-C hybrid catalyst suggesting the possibility of the strengthened nanoparticle-support interaction. An important note however, is that the M-N-C materials made in the fashion of a sacrificial support method may not be the ideal support system for degradation improvements as the graphitization amount is typically lower than other types of carbon-based supports (such as Vulcan carbon blacks and metal-organic-framework-based M-N-C materials).[157,158]

5.8 Conclusions

In summary, we've synthesized a collection of M-N-C catalysts and test them with and without Pt nanoparticles to build a periodic trend for the oxygen reduction and carbon monoxide oxidation reactions. From our tests, we found volcano-type trends for the bare and hybrid catalysts towards the oxygen reduction reaction and linear-type trends towards the carbon monoxide oxidation reaction. The results strongly suggest that the interactions that occur between the Pt nanoparticles and the M-N-C support materials is likely due to the changes in the atomically dispersed metal dopant elements. Although the mechanism is still unknown, it's possible that the electrostatics of the carbon support surface may change with altering the metal dopants which can have a significant impact on the surface properties of the Pt nanoparticles. From these results, it would be expected that an ideal multimetallic M-N-C

material could be formulated to change the electrostatics in a way that may improve the activity and durability of the Pt nanoparticles.

6. Conclusions and Outlook

The conclusions of this work can be split into the follow sections: (1) nanoparticle-support interactions, (2) nanoparticle-ionomer interactions, and (3) support-ionomer interactions. From the work in chapter 3, we hypothesized and examined a few of the important interactions between the active nanoparticles, the carbon support, and the ion conducting material. Based on previous works, we expected that the introduction of porous (or advanced structured) nanostructures may lead to issues of either mass transport or electric conductivity to the active sites and that the ionomer structure in a solid-state system would be highly inefficient in covering the catalyst powder. We proposed the following: (1) the ion conducting material should be tailored in a way that can allow for consistent coverage of the catalyst, (2) the nanoparticles should be designed in a way that all active sites can be easily accessible, and (3) the introduction of a "buffer" layer (likely being ionic liquids) can mediate the issues of mass transport toward the active sites.

In chapter 4, a novel nanostructure (the nanoflower) was characterized and integrated into an MEA to understand the challenges of designing and integrating porous structures in a solid-state system. What we found through characterization of the nanoflower structure was that the nanoflowers were largely monocrystalline thus leading to small amounts of microstrain and surface distortion. These findings corroborating with the improved activity in RDE testing suggested that the nanoflowers had active sites that exhibited far greater activities than others, however these improvements were lost when transferring to fuel cell tests. It seems that regardless of how the catalyst layer is prepared that the mass transport losses dominate in the solid state and that porous nanostructures should be avoided. In addition, the monocrystallinity of the

nanostructure did not aid in the longevity of the catalyst and the porous structure collapsed quickly when going through operating procedures. In a positive note, the novel carbon monoxide cleaning protocol was able to remove tightly bound organics from all active surfaces of the nanoflowers and is a procedure that can be applied to most platinum-based nanostructures.

In chapter 5, a library of metal-nitrogen-carbon materials was tested for its ORR activity as well as its usage as an active support for platinum-based nanoparticles. We found through the testing for the oxygen reduction reaction and the carbon monoxide oxidation that the active site (or surface) behavior changed dramatically depending on the single atom element that was doped into the carbon support. We were able to draw periodic trends (either linear or parabolic) of both reactions based on the doping elements. These results serve as a baseline for carbon support design in which the surface energetics of the active nanoparticles can be tuned by the tuning of the carbon supports.

From the results of this work, we would speculate that the next steps for development center around the ion conducting material design as well as the support material design. Nanostructures of all types still have issues with complete ionomer coverage and also suffer from the inverse relationship of either adequate proton conductivity or oxygen gas transport which could be mediated by a buffer layer (i.e., ionic liquids layer). Typical carbon black supports offer only electron conductivity, however different surface functionalization or materials doping could allow the carbon supports to improve activity and durability. More work must be done on understanding the effects that the support material can have on the catalytic sites of the supported nanoparticles. The development of pure M-N-C catalysts will also benefit from the understanding of the ionomer-catalyst interfaces and the carbon modifications, which could lead to PGM-free catalysts that can excess industry standards in the near future.

7. References

1. U.S. energy facts explained - consumption and production - U.S. Energy Information Administration (EIA). https://www.eia.gov/energyexplained/us-energy-facts/.

2. US EPA, O. Sources of Greenhouse Gas Emissions. *US EPA* https://www.epa.gov/ghgemissions/sources-greenhouse-gas-emissions (2015).

3. Fan, J. *et al.* Bridging the gap between highly active oxygen reduction reaction catalysts and effective catalyst layers for proton exchange membrane fuel cells. *Nat Energy* **6**, 475–486 (2021).

4. Li, Y. *et al.* Recent Progresses in Oxygen Reduction Reaction Electrocatalysts for Electrochemical Energy Applications. *Electrochem. Energ. Rev.* **2**, 518–538 (2019).

5. Asset, T. & Atanassov, P. Iron-Nitrogen-Carbon Catalysts for Proton Exchange Membrane Fuel Cells. *Joule* **4**, 33–44 (2020).

6. Davydova, E. S., Mukerjee, S., Jaouen, F. & Dekel, D. R. Electrocatalysts for Hydrogen Oxidation Reaction in Alkaline Electrolytes. *ACS Catal.* **8**, 6665–6690 (2018).

7. Shin, D. *et al.* Reduced formation of peroxide and radical species stabilises iron-based hybrid catalysts in polymer electrolyte membrane fuel cells. *Journal of Energy Chemistry* **65**, 433–438 (2022).

8. Mechler, A. K. *et al.* Stabilization of Iron-Based Fuel Cell Catalysts by Non-Catalytic Platinum. *Journal of The Electrochemical Society* **165**, 1084–1091 (2018).

9. Ly, A., Asset, T. & Atanassov, P. Integrating nanostructured Pt-based electrocatalysts in proton exchange membrane fuel cells. *Journal of Power Sources* **478**, 228516 (2020).

10. Ohyama, J. *et al.* High Durability of a 14-Membered Hexaaza Macrocyclic Fe Complex for an Acidic Oxygen Reduction Reaction Revealed by In Situ XAS Analysis. *JACS Au* **1**, 1798–1804 (2021).

11. Artyushkova, K. *et al.* Correlations between Synthesis and Performance of Fe-Based PGM-Free Catalysts in Acidic and Alkaline Media: Evolution of Surface Chemistry and Morphology. *ACS Appl. Energy Mater.* **2**, 5406–5418 (2019).

12.   Rezaei Talarposhti, M. *et al.* Kinetic Isotope Effect as a Tool To Investigate the Oxygen Reduction

Reaction on Pt-based Electrocatalysts – Part II: Effect of Platinum Dispersion. *ChemPhysChem* **21**,

1331–1339 (2020).

13.   Huang, S.-Y., Ganesan, P., Park, S. & Popov, B. N. Development of a Titanium Dioxide-Supported

Platinum Catalyst with Ultrahigh Stability for Polymer Electrolyte Membrane Fuel Cell Applications. *J.

Am. Chem. Soc.* **131**, 13898–13899 (2009).

14.   Zhang, P., Huang, S.-Y. & Popov, B. N. Mesoporous Tin Oxide as an Oxidation-Resistant Catalyst

Support for Proton Exchange Membrane Fuel Cells. *J. Electrochem. Soc.* **157**, B1163 (2010).

15.   Chen, M. *et al.* High-Platinum-Content Catalysts on Atomically Dispersed and Nitrogen

Coordinated Single Manganese Site Carbons for Heavy-Duty Fuel Cells. *J. Electrochem. Soc.* **169**,

034510 (2022).

16.   Qiao, Z. *et al.* Atomically dispersed single iron sites for promoting Pt and Pt3Co fuel cell

catalysts: performance and durability improvements. *Energy Environ. Sci.* (2021)

doi:10.1039/D1EE01675J.

17.   Liang, L. *et al.* Cobalt single atom site isolated Pt nanoparticles for efficient ORR and HER in acid

media. *Nano Energy* **88**, 106221 (2021).

18.   Liang, L. *et al.* Ultra-small platinum nanoparticles segregated by nickle sites for efficient ORR and

HER processes. *Journal of Energy Chemistry* **65**, 48–54 (2022).

19.   Meier, J. C. *et al.* Design criteria for stable Pt/C fuel cell catalysts. *Beilstein J. Nanotechnol.* **5**, 44–

67 (2014).

20.   Lopes, P. P. *et al.* Eliminating dissolution of platinum-based electrocatalysts at the atomic scale.

Nat. Mater. **19**, 1207–1214 (2020).

21.   Hornberger, E. *et al.* Impact of Carbon N-Doping and Pyridinic-N Content on the Fuel Cell

Performance and Durability of Carbon-Supported Pt Nanoparticle Catalysts. *ACS Appl. Mater.*

Interfaces (2022) doi:10.1021/acsami.2c00762.

22.   Asset, T. *et al.* Activity and Durability of Platinum-Based Electrocatalysts Supported on Bare or

Fluorinated Nanostructured Carbon Substrates. *J. Electrochem. Soc.* **165**, F3346–F3358 (2018).

23.   Yu, X. & Ye, S. Recent advances in activity and durability enhancement of Pt/C catalytic cathode

in PEMFC: Part I. Physico-chemical and electronic interaction between Pt and carbon support, and

activity enhancement of Pt/C catalyst. *Journal of Power Sources* **172**, 133–144 (2007).

24.   Castanheira, L. *et al.* Carbon Corrosion in Proton-Exchange Membrane Fuel Cells: From Model

Experiments to Real-Life Operation in Membrane Electrode Assemblies. *ACS Catal.* **4**, 2258–2267

(2014).

25.   Oh, H.-S. & Kim, H. Efficient Synthesis of Pt Nanoparticles Supported on Hydrophobic

Graphitized Carbon Nanofibers for Electrocatalysts Using Noncovalent Functionalization. *Advanced*

Functional Materials **21**, 3954–3960 (2011).

26.   U.S. EIA. *Annual Energy Outlook 2019 with projections to 2050*. *Annual Energy Outlook 2019*

with projections to 2050 (2019) doi:DOE/EIA-0383(2012) U.S.

27.   Gasteiger, H. A., Kocha, S. S., Sompalli, B. & Wagner, F. T. Activity benchmarks and requirements

for Pt, Pt-alloy, and non-Pt oxygen reduction catalysts for PEMFCs. *Applied Catalysis B: Environmental*

56, 9–35 (2005).

28.   Nørskov, J. K. *et al.* Origin of the Overpotential for Oxygen Reduction at a Fuel-Cell Cathode. *The*

Journal of Physical Chemistry B **108**, 17886–17892 (2004).

29.   Stephens, I. E. L., Bondarenko, A. S., Grønbjerg, U., Rossmeisl, J. & Chorkendorff, I.

Understanding the electrocatalysis of oxygen reduction on platinum and its alloys. *Energy &*

Environmental Science **5**, 6744–6762 (2012).

30.   Locating the World's Minerals and Mines. http://www.mining.com/infographic-where-the-minerals-are-82638/.

31.   Lefevre, M., Proietti, E., Jaouen, F. & Dodelet, J.-P. Iron-Based Catalysts with Improved Oxygen Reduction Activity in Polymer Electrolyte Fuel Cells. *Science* **324**, 71–74 (2009).

32.   Jaouen, F. *et al.* Recent advances in non-precious metal catalysis for oxygen-reduction reaction in polymer electrolyte fuel cells. *Energy & Environmental Science* **4**, 114–130 (2011).

33.   Wu, G., More, K. L., Johnston, C. M. & Zelenay, P. High-Performance Electrocatalysts for Oxygen Reduction Derived from Polyaniline, Iron and Cobalt. *Science* **332**, 443–447 (2011).

34.   Jaouen, F. *et al.* Cross-laboratory experimental study of non-noble-metal electrocatalysts for the oxygen reduction reaction. *ACS Applied Materials and Interfaces* **1**, 1623–1639 (2009).

35.   Kitchin, J. R., Nørskov, J. K., Barteau, M. A. & Chen, J. G. Modification of the surface electronic and chemical properties of Pt (111) by subsurface 3d transition metals. *The Journal of Chemical Physics* **120**, 10240–10246 (2004).

36.   Viswanathan, V., Hansen, H. A., Rossmeisl, J. & Nørskov, J. K. Universality in Oxygen Reduction Electrocatalysis on Metal Surfaces. *ACS Catalysis* **2**, 1654–1660 (2012).

37.   Bligaard, T. & Nørskov, J. K. Ligand effects in heterogeneous catalysis and electrochemistry. *Electrochimica Acta* **52**, 5512–5516 (2007).

38.   Greeley, J. & Nørskov, J. K. Combinatorial Density Functional Theory-Based Screening of Surface Alloys for the Oxygen Reduction Reaction. *The Journal of Physical Chemistry C* **113**, 4932–4939 (2009).

39.   Mavrikakis, M., Hammer, B. & Norskov, J. K. Effect of strain on the reactivity of metal surfaces. *Physical Review Letters* **81**, 2819–2822 (1998).

40.   Strasser, P. *et al.* Lattice-strain control of the activity in dealloyed core-shell fuel cell catalysts. *Nat Chem* **2**, 454–460 (2010).

41.   Zhang, J., Vukmirovic, M. B., Xu, Y., Mavrikakis, M. & Adzic, R. R. Controlling the catalytic activity of platinum-monolayer electrocatalysts for oxygen reduction with different substrates. *Angew. Chem., Int. Ed.* **44**, 2132–2135 (2005).

42.   Cui, C. *et al.* Octahedral PtNi nanoparticle catalysts: exceptional oxygen reduction activity by tuning the alloy particle surface composition. *Nano Letters* **12**, 5885–5889 (2012).

43.   Stamenkovic, V. R. *et al.* Improved oxygen reduction activity on Pt3Ni (111) via increased surface site availability. *Science* **315**, 493–497 (2007).

44.   Calle-Vallejo, F. *et al.* Finding optimal surface sites on heterogeneous catalysts by counting nearest neighbors. *Science* **350**, 185–189 (2015).

45.   Calle-Vallejo, F., Martínez, J. I., García-Lastra, J. M., Sautet, P. & Loffreda, D. Fast prediction of adsorption properties for platinum nanocatalysts with generalized coordination numbers. *Angew. Chem., Int. Ed.* **53**, 8316–8319 (2014).

46.   Le Bacq, O. *et al.* Effect of Atomic Vacancies on the Structure and the Electrocatalytic Activity of Pt-rich/C Nanoparticles: A Combined Experimental and Density Functional Theory Study. *ChemCatChem* **9**, 2324–2338 (2017).

47.   Chen, C. *et al.* Highly Crystalline Multimetallic Nanoframes with Three-Dimensional Electrocatalytic Surfaces. *Science* **343**, 1339–1343 (2014).

48.   Mccue, I., Snyder, J., Livi, K. & Erlebacher, J. Structure / Processing / Properties Relationships in Nanoporous Nanoparticles As Applied to Catalysis of the Cathodic Oxygen Reduction Reaction Structure / Processing / Properties Relationships in Nanoporous Nanoparticles As Applied to Catalysis of the Ca. (2012) doi:10.1021/ja3019498.

49.   Dubau, L. *et al.* Tuning the Performance and the Stability of Porous Hollow PtNi/C Nanostructures for the Oxygen Reduction Reaction. *ACS Catalysis* **5**, 5333–5341 (2015).

50.   Li, M. *et al.* Ultrafine jagged platinum nanowires enable ultrahigh mass activity for the oxygen reduction reaction. *Science* **354**, 1414–1419 (2016).

51.   Stamenkovic, V. R. & Markovic, N. M. Nanosegregated Cathode Alloy Catalysts with Ultra-Low Platinum Loading. in *DOE Hydrogen and Fuel Cells Program* V13–V19 (2015).

52.   Mauger, S. A. *et al.* Fuel Cell Performance Implications of Membrane Electrode Assembly Fabrication with Platinum-Nickel Nanowire Catalysts. *Journal of The Electrochemical Society* **165**, 238–245 (2018).

53.   Paulus, U. A. *et al.* Oxygen reduction on high surface area Pt-based alloy catalysts in comparison to well defined smooth bulk alloy electrodes. *Electrochimica Acta* **47**, 3787–3798 (2002).

54.   Adzic, R. R. *et al.* Platinum monolayer fuel cell electrocatalysts. *Topics in Catalysis* **46**, 249–262 (2007).

55.   Mani, P., Srivastava, R. & Strasser, P. Dealloyed binary PtM3 (M=Cu, Co, Ni) and ternary PtNi3M (M=Cu, Co, Fe, Cr) electrocatalysts for the oxygen reduction reaction: Performance in polymer electrolyte membrane fuel cells. *Journal of Power Sources* **196**, 666–673 (2011).

56.   Gan, L., Cui, C., Rudi, S. & Strasser, P. Core-shell and nanoporous particle architectures and their effect on the activity and stability of Pt ORR electrocatalysts. *Topics in Catalysis* **57**, 236–244 (2014).

57.   Pedersen, A. F. *et al.* Probing the nanoscale structure of the catalytically active overlayer on Pt alloys with rare earths. *Nano Energy* **29**, 249–260 (2016).

58.   Ulrikkeholm, E. T. *et al.* PtxGd alloy formation on Pt(111): Preparation and structural characterization. *Surface Science* **652**, 114–122 (2016).

59.   Escudero-Escribano, M. *et al.* Tuning the activity of Pt alloy electrocatalysts by means of the lanthanide contraction. *Science* **352**, 73–76 (2016).

60.   Suo, Y., Zhuang, L. & Lu, J. First-principles considerations in the design of Pd-alloy catalysts for oxygen reduction. *Angew. Chem., Int. Ed.* **46**, 2862–2864 (2007).

61.   Stamenkovic, V. R. *et al.* Trends in electrocatalysis on extended and nanoscale Pt-bimetallic alloy surfaces. *Nature Materials* **6**, 241–247 (2007).

62.   Stamenkovic, V. R. & Marković, N. M. Nanosegregated Cathode Alloy Catalysts with Ultra-Low Platinum Loading. in *DOE Hydrogen and Fuel Cells Program* V13–V19 (2015).

63.   Oezaslan, M., Hasché, F. & Strasser, P. Pt-Based Core–Shell Catalyst Architectures for Oxygen Fuel Cell Electrodes. *The Journal of Physical Chemistry Letters* **4**, 3273–3291 (2013).

64.   Oezaslan, M., Heggen, M. & Strasser, P. Size-Dependent morphology of dealloyed bimetallic catalysts: Linking the nano to the macro scale. *Journal of the American Chemical Society* **134**, 514–524 (2012).

65.   Wang, D. *et al.* Structurally ordered intermetallic platinum–cobalt core–shell nanoparticles with enhanced activity and stability as oxygen reduction electrocatalysts. *Nature Materials* **12**, 81–87 (2012).

66.   Cui, C., Gan, L., Heggen, M., Rudi, S. & Strasser, P. Compositional segregation in shaped Pt alloy nanoparticles and their structural behaviour during electrocatalysis. *Nature materials* **12**, 765–771 (2013).

67.   Čolić, V. & Bandarenka, A. S. Pt Alloy Electrocatalysts for the Oxygen Reduction Reaction: From Model Surfaces to Nanostructured Systems. *ACS Catalysis* **6**, 5378–5385 (2016).

68.   Markovic, N. M., Adzic, R. R., Cahan, B. D. & Yeager, E. B. Structural effects in electrocatalysis - oxygen reduction on platinum low-index single-crystal surfaces in perchloric-acid solutions. *Journal of Electroanalytical Chemistry* **377**, 249–259 (1994).

69.   Li, B. *et al.* High performance octahedral PtNi / C catalysts investigated from rotating disk electrode to membrane electrode assembly. *Nano Research* **12**, 281–287 (2019).

70.   Huang, X. *et al.* High-performance transition metal – doped Pt3Ni octahedra for oxygen reduction reaction. *Science* **348**, 1230–1234 (2015).

71.   Beermann, V. *et al.* Rh-Doped Pt-Ni Octahedral Nanoparticles: Understanding the Correlation

        between Elemental Distribution, Oxygen Reduction Reaction, and Shape Stability. *Nano letters* **16**,

        1719–1725 (2016).

72.   Kuzume, A., Herrero, E. & Feliu, J. M. Oxygen reduction on stepped platinum surfaces in acidic

        media. *Journal of Electroanalytical Chemistry* **599**, 333–343 (2007).

73.   Hitotsuyanagi, A., Nakamura, M. & Hoshi, N. Structural effects on the activity for the oxygen

        reduction reaction on n(111)–(100) series of Pt: correlation with the oxide film formation.

        Electrochimica Acta **82**, 512–516 (2012).

74.   Bandarenka, A. S., Hansen, H., Rossmeisl, J. & Stephens, I. E. L. Elucidating the activity of stepped

        Pt single crystals for oxygen reduction. *Physical chemistry chemical physics : PCCP* **16**, 13625–13629

        (2014).

75.   Pohl, M. D., Colic, V., Scieszka, D. & Bandarenka, A. S. Elucidation of adsorption processes at the

        surface of Pt(331) model electrocatalysts in acidic aqueous media. *Phys. Chem. Chem. Phys.* **18**,

        10792–10799 (2016).

76.   Qin, W. & Szpunar, J. A. Origin of lattice strain in nanocrystalline materials. *Philosophical

        Magazine Letters* **85**, 649–656 (2005).

77.   Qin, W., Nagase, T., Umakoshi, Y. & Szpunar, J. A. Relationship between microstrain and lattice

        parameter change in nanocrystalline materials. *Philosophical Magazine Letters* **88**, 169–179 (2008).

78.   Chattot, R. *et al.* Beyond Alloying Effects: Microstrain-Induced Enhancement of the Oxygen

        Reduction Reaction Kinetics on Various PtNi/C Nanostructures. *ACS Catalysis* **7**, 398–408 (2017).

79.   Chattot, R. *et al.* Surface distortion as a unifying concept and descriptor in oxygen reduction

        reaction electrocatalysis. *Nature Materials* **17**, 827–833 (2018).

80.   Shao, M., Peles, A. & Shoemaker, K. Electrocatalysis on Platinum Nanoparticles : Particle Size

        Effect on Oxygen Reduction Reaction Activity. *Nano letters* **11**, 3714–3719 (2011).

81.   Zhang, J. *et al.* Platinum monolayer on nonnoble metal-noble metal core-shell nanoparticle electrocatalysts for O2 reduction. *Journal of Physical Chemistry B* **109**, 22701–22704 (2005).

82.   Zhang, Y. *et al.* Hollow core supported Pt monolayer catalysts for oxygen reduction. *Catalysis Today* **202**, 50–54 (2013).

83.   Snyder, J., McCue, I., Livi, K. & Erlebacher, J. Structure/Processing/Properties relationships in nanoporous nanoparticles as applied to catalysis of the cathodic oxygen reduction reaction. *Journal of the American Chemical Society* **134**, 8633–8645 (2012).

84.   Pan, L., Ott, S., Dionigi, F. & Strasser, P. Current challenges related to the deployment of shape-controlled Pt alloy oxygen reduction reaction nanocatalysts into low Pt-loaded cathode layers of proton exchange membrane fuel cells. *Current Opinion in Electrochemistry* **18**, 61–71 (2019).

85.   Lopez-Haro, M. *et al.* Three-dimensional analysis of Nafion layers in fuel cell electrodes. *Nature communications* **5**, 5229–5334 (2014).

86.   Karan, K. PEFC catalyst layer: Recent advances in materials, microstructural characterization, and modeling. *Current Opinion in Electrochemistry* **5**, 27–35 (2017).

87.   Uchida, M., Aoyama, Y., Eda, N. & Ohta, A. Investigation of the Microstructure in the Catalyst Layer and Effects of Both Perfluorosulfonate Ionomer and PTFE-Loaded Carbon on the Catalyst Layer of Polymer Electrolyte Fuel Cells. *Journal of the Electrochemical Society* **142**, 4143–4149 (1995).

88.   Ngo, T. T., Yu, T. L. & Lin, H. L. Influence of the composition of isopropyl alcohol/water mixture solvents in catalyst ink solutions on proton exchange membrane fuel cell performance. *Journal of Power Sources* **225**, 293–303 (2013).

89.   Ngo, T. T., Yu, T. L. & Lin, H. L. Nafion-based membrane electrode assemblies prepared from catalyst inks containing alcohol/water solvent mixtures. *Journal of Power Sources* **238**, 1–10 (2013).

90.   Uchida, M., Aoyama, Y., Eda, N. & Ohta, A. New Preparation Method for Polymer-Electrolyte Fuel Cells. *Journal of the Electrochemical Society* **142**, 463–468 (1995).

91.   Liu, J. & Zenyuk, I. V. Proton transport in ionomer-free regions of polymer electrolyte fuel cells and implications for oxygen reduction reaction. *Current Opinion in Electrochemistry* **12**, 202–208 (2018).

92.   Huang, J., Malek, A., Zhang, J. & Eikerling, M. H. Non-monotonic Surface Charging Behavior of Platinum: A Paradigm Change. *Journal of Physical Chemistry C* **120**, 13587–13595 (2016).

93.   Harzer, G. S., Orfanidi, A., El-Sayed, H., Madkikar, P. & Gasteiger, H. A. Tailoring catalyst morphology towards high performance for low Pt loaded PEMFC cathodes. *Journal of the Electrochemical Society* **165**, F770–F779 (2018).

94.   Yang, L. *et al.* Activity, Performance, and Durability for the Reduction of Oxygen in PEM Fuel Cells, of Fe/N/C Electrocatalysts Obtained from the Pyrolysis of Metal-Organic-Framework and Iron Porphyrin Precursors. *Electrochimica Acta* **159**, 184–197 (2015).

95.   Kodama, K. *et al.* Effect of the Side-Chain Structure of Perfluoro-Sulfonic Acid Ionomers on the Oxygen Reduction Reaction on the Surface of Pt. *ACS Catalysis* **8**, 694–700 (2018).

96.   Jinnouchi, R., Kudo, K., Kitano, N. & Morimoto, Y. Molecular Dynamics Simulations on O2 Permeation through Nafion Ionomer on Platinum Surface. *Electrochimica Acta* **188**, 767–776 (2016).

97.   Kusoglu, A. & Weber, A. Z. New Insights into Perfluorinated Sulfonic-Acid Ionomers. *Chemical Reviews* **117**, 987–1104 (2017).

98.   Schuler, T. *et al.* Fuel-cell catalyst-layer resistance via hydrogen limiting-current measurements. *Journal of the Electrochemical Society* **166**, F3020–F3031 (2019).

99.   Martínez-Hincapié, R., Climent, V. & Feliu, J. M. Peroxodisulfate reduction as a probe to interfacial charge. *Electrochemistry Communications* **88**, 43–46 (2018).

100.   Martínez-Hincapié, R., Climent, V. & Feliu, J. M. New probes to surface free charge at electrochemical interfaces with platinum electrodes. *Current Opinion in Electrochemistry* **14**, 16–22 (2019).

101.   Van Cleve, T. *et al.* Dictating Pt-Based Electrocatalyst Performance in Polymer Electrolyte Fuel

        Cells, from Formulation to Application. *ACS Applied Materials and Interfaces* (2019)

        doi:10.1021/acsami.9b17614.

102.   Garsany, Y., Atkinson, R. W., Gould, B. D. & Swider-Lyons, K. E. High power, Low-Pt membrane

        electrode assemblies for proton exchange membrane fuel cells. *Journal of Power Sources* **408**, 38–45

        (2018).

103.   Orfanidi, A. *et al.* The key to high performance low pt loaded electrodes. *Journal of the*

        Electrochemical Society **164**, F418–F426 (2017).

104.   Castanheira, L. *et al.* Carbon Corrosion in Proton-Exchange Membrane Fuel Cells: From Model

        Experiments to Real-Life Operation in Membrane Electrode Assemblies. *ACS Catalysis* **4**, 2258–2267

        (2014).

105.   Shao, Y., Sui, J., Yin, G. & Gao, Y. Nitrogen-doped carbon nanostructures and their composites as

        catalytic materials for proton exchange membrane fuel cell. *Applied Catalysis B: Environmental* **79**,

        89–99 (2008).

106.   Watanabe, M. & Tryk, D. A. *The Role of Carbon Blacks as Catalyst Supports and Structural*

        Elements in Polymer Electrolyte Fuel Cells. (Springer International Publishing, 2019). doi:10.1007/978-

        3-319-92917-0_4.

107.   Snyder, J., Livi, K. & Erlebacher, J. Oxygen Reduction Reaction Performance of [MTBD][beti]-

        Encapsulated Nanoporous NiPt Alloy Nanoparticles. *Advanced Functional Materials* **23**, 5494–5501

        (2013).

108.   Benn, E., Uvegi, H. & Erlebacher, J. Characterization of nanoporous metal-ionic liquid composites

        for the electrochemical oxygen reduction reaction. *Journal of the Electrochemical Society* **162**, H759–

        H766 (2015).

109.   Huang, K., Song, T., Morales-Collazo, O., Jia, H. & Brennecke, J. F. Enhancing Pt/C catalysts for

the oxygen reduction reaction with protic ionic liquids: The effect of anion structure. *Journal of the*

Electrochemical Society **164**, F1448–F1459 (2017).

110.   Pozo-Gonzalo, C. Oxygen Reduction Reaction in Ionic Liquids: An Overview. in *Electrochemistry*

in Ionic Liquids (ed. Torriero, A. A. J.) 507–529 (Springer, 2015). doi:10.1007/978-3-319-15132-8.

111.   Zhang, Y. & Pozo-Gonzalo, C. Variations and applications of the oxygen reduction reaction in

ionic liquids. *Chemical Communications* **54**, 3800–3810 (2018).

112.   Switzer, E. E. *et al.* Oxygen reduction reaction in ionic liquids: The addition of protic species.

Journal of Physical Chemistry C **117**, 8683–8690 (2013).

113.   Greeley, J. *et al.* Alloys of platinum and early transition metals as oxygen reduction

electrocatalysts. *Nature Chemistry* **1**, 552–556 (2009).

114.   Pan, L., Ott, S., Dionigi, F. & Strasser, P. Current challenges related to the deployment of shape-

controlled Pt alloy oxygen reduction reaction nanocatalysts into low Pt-loaded cathode layers of

proton exchange membrane fuel cells. *Current Opinion in Electrochemistry* **18**, 61–71 (2019).

115.   Moriau, L. J. *et al.* Resolving the nanoparticles' structure-property relationships at the atomic

level: a study of Pt-based electrocatalysts. *iScience* **24**, 102102 (2021).

116.   Zhang, J. *et al.* Stabilizing Pt-Based Electrocatalysts for Oxygen Reduction Reaction: Fundamental

Understanding and Design Strategies. *Advanced Materials* **n/a**, 2006494.

117.   Xia, W., Mahmood, A., Liang, Z., Zou, R. & Guo, S. Earth-Abundant Nanomaterials for Oxygen

Reduction. *Angewandte Chemie International Edition* **55**, 2650–2676 (2016).

118.   Rudi, S., Cui, C., Gan, L. & Strasser, P. Comparative Study of the Electrocatalytically Active

Surface Areas (ECSAs) of Pt Alloy Nanoparticles Evaluated by Hupd and CO-stripping voltammetry. 13.

119.   Li, M. *et al.* Ultrafine jagged platinum nanowires enable ultrahigh mass activity for the oxygen

reduction reaction. *Science* **354**, 1414–1419 (2016).

120.   Cui, C. *et al.* Octahedral PtNi Nanoparticle Catalysts: Exceptional Oxygen Reduction Activity by Tuning the Alloy Particle Surface Composition. *Nano Lett.* **12**, 5885–5889 (2012).

121.   Stamenkovic, V. R. *et al.* Trends in electrocatalysis on extended and nanoscale Pt-bimetallic alloy surfaces. *Nature Materials* **6**, 241–247 (2007).

122.   Stamenkovic, V. R. *et al.* Improved Oxygen Reduction Activity on Pt3Ni(111) via Increased Surface Site Availability. *Science* **315**, 493–497 (2007).

123.   K. Chaudhari, N. *et al.* Recent advances in electrocatalysts toward the oxygen reduction reaction: the case of PtNi octahedra. *Nanoscale* **10**, 20073–20088 (2018).

124.   Li, B. *et al.* High performance octahedral PtNi/C catalysts investigated from rotating disk electrode to membrane electrode assembly. *Nano Res.* **12**, 281–287 (2019).

125.   Wang, C. *et al.* Synthesis of Homogeneous Pt-Bimetallic Nanoparticles as Highly Efficient Electrocatalysts. *ACS Catal.* **1**, 1355–1359 (2011).

126.   Tian, X. *et al.* Engineering bunched Pt-Ni alloy nanocages for efficient oxygen reduction in practical fuel cells. *Science* **366**, 850–856 (2019).

127.   Snyder, J., McCue, I., Livi, K. & Erlebacher, J. Structure/Processing/Properties Relationships in Nanoporous Nanoparticles As Applied to Catalysis of the Cathodic Oxygen Reduction Reaction. *J. Am. Chem. Soc.* **134**, 8633–8645 (2012).

128.   Dubau, L. *et al.* Tuning the Performance and the Stability of Porous Hollow PtNi/C Nanostructures for the Oxygen Reduction Reaction. *ACS Catal.* **5**, 5333–5341 (2015).

129.   Chen, C. *et al.* Highly Crystalline Multimetallic Nanoframes with Three-Dimensional Electrocatalytic Surfaces. *Science* **343**, 1339–1343 (2014).

130.   Chattot, R. *et al.* Beyond Strain and Ligand Effects: Microstrain-Induced Enhancement of the Oxygen Reduction Reaction Kinetics on Various PtNi/C Nanostructures. *ACS Catal.* **7**, 398–408 (2017).

131.   Chattot, R. *et al.* Surface distortion as a unifying concept and descriptor in oxygen reduction

reaction electrocatalysis. *Nature Materials* **17**, 827 (2018).

132.   Calle-Vallejo, F. *et al.* Finding optimal surface sites on heterogeneous catalysts by counting

nearest neighbors. *Science* **350**, 185–189 (2015).

133.   Bacq, O. L. *et al.* Effect of Atomic Vacancies on the Structure and the Electrocatalytic Activity of

Pt-rich/C Nanoparticles: A Combined Experimental and Density Functional Theory Study.

ChemCatChem **9**, 2324–2338 (2017).

134.   Gong, K., Vukmirovic, M. B., Ma, C., Zhu, Y. & Adzic, R. R. Synthesis and catalytic activity of Pt

monolayer on Pd tetrahedral nanocrystals with CO-adsorption-induced removal of surfactants.

Journal of Electroanalytical Chemistry **662**, 213–218 (2011).

135.   Tsuji, M. *et al.* Toward to branched platinum nanoparticles by polyol reduction: A role of

poly(vinylpyrrolidone) molecules. *Colloids and Surfaces A: Physicochemical and Engineering Aspects*

317, 23–31 (2008).

136.   Safo, I. A., Dosche, C. & Oezaslan, M. TEM, FTIR and Electrochemistry Study: Desorption of PVP

from Pt Nanocubes. *Zeitschrift für Physikalische Chemie* **232**, 1319–1333 (2018).

137.   Yin, J., Wang, J., Li, M., Jin, C. & Zhang, T. Iodine Ions Mediated Formation of Monomorphic

Single-Crystalline Platinum Nanoflowers. *Chem. Mater.* **24**, 2645–2654 (2012).

138.   Li, J. *et al.* Synthesis of Platinum Nanocrystals within Iodine Ions Mediated. *Journal of

Nanomaterials* https://www.hindawi.com/journals/jnm/2018/1465760/ (2018)

doi:10.1155/2018/1465760.

139.   Oh, H.-S., Oh, J.-G., Hong, Y.-G. & Kim, H. Investigation of carbon-supported Pt nanocatalyst

preparation by the polyol process for fuel cell applications. *Electrochimica Acta* **52**, 7278–7285

(2007).

140. Oh, H.-S., Oh, J.-G. & Kim, H. Modification of polyol process for synthesis of highly platinum loaded platinum–carbon catalysts for fuel cells. *Journal of Power Sources* **183**, 600–603 (2008).

141. Tabatabaei, K. *et al.* Halogen-Induced Crystallinity and Size Tuning of Microwave Synthesized Germanium Nanocrystals. *Chem. Mater.* **31**, 7510–7521 (2019).

142. Xiang Chen, W., Yang Lee, J. & Liu, Z. Microwave-assisted synthesis of carbon supported Pt nanoparticles for fuel cell applications. *Chemical Communications* **0**, 2588–2589 (2002).

143. Harada, M. & Cong, C. Microwave-Assisted Polyol Synthesis of Polymer-Protected Monometallic Nanoparticles Prepared in Batch and Continuous-Flow Processing. *Ind. Eng. Chem. Res.* **55**, 5634–5643 (2016).

144. Kundu, P. *et al.* Ultrafast Microwave-Assisted Route to Surfactant-Free Ultrafine Pt Nanoparticles on Graphene: Synergistic Co-reduction Mechanism and High Catalytic Activity. *Chem. Mater.* **23**, 2772–2780 (2011).

145. Cheong, S., Watt, J., Ingham, B., Toney, M. F. & Tilley, R. D. In Situ and Ex Situ Studies of Platinum Nanocrystals: Growth and Evolution in Solution. *J. Am. Chem. Soc.* **131**, 14590–14595 (2009).

146. Marinkovic, N., Sasaki, K. & Adzic, R. Nanoparticle size evaluation of catalysts by EXAFS: Advantages and limitations. *Zas Mat* **57**, 101–109 (2016).

147. Long, N. V., Ohtaki, M., Nogami, M. & Hien, T. D. Effects of heat treatment and poly(vinylpyrrolidone) (PVP) polymer on electrocatalytic activity of polyhedral Pt nanoparticles towards their methanol oxidation. *Colloid Polym Sci* **289**, 1373–1386 (2011).

148. Cai, X., Lin, R., Liu, X. & Zhao, Y. Effect of heat treatment on the surface structure of Pd@Pt–Ni core-shell catalysts for the oxygen reduction reaction. *Journal of Alloys and Compounds* **884**, 161059 (2021).

149.   Bezerra, C. W. B. *et al.* A review of heat-treatment effects on activity and stability of PEM fuel cell catalysts for oxygen reduction reaction. *Journal of Power Sources* **173**, 891–908 (2007).

150.   Maillard, F. *et al.* Influence of particle agglomeration on the catalytic activity of carbon-supported Pt nanoparticles in CO monolayer oxidation. *Phys. Chem. Chem. Phys.* **7**, 385–393 (2005).

151.   Lefèvre, M., Proietti, E., Jaouen, F. & Dodelet, J.-P. Iron-Based Catalysts with Improved Oxygen Reduction Activity in Polymer Electrolyte Fuel Cells. *Science* **324**, 71–74 (2009).

152.   Yang, X., Priest, C., Hou, Y. & Wu, G. Atomically dispersed dual-metal-site PGM-free electrocatalysts for oxygen reduction reaction: Opportunities and challenges. *SusMat* **n/a**,.

153.   Han, L. *et al.* A single-atom library for guided monometallic and concentration-complex multimetallic designs. *Nat. Mater.* **21**, 681–688 (2022).

154.   Qin, J. *et al.* Altering Ligand Fields in Single-Atom Sites through Second-Shell Anion Modulation Boosts the Oxygen Reduction Reaction. *J. Am. Chem. Soc.* **144**, 2197–2207 (2022).

155.   Nørskov, J. K. *et al.* Origin of the Overpotential for Oxygen Reduction at a Fuel-Cell Cathode. *J. Phys. Chem. B* **108**, 17886–17892 (2004).

156.   Artyushkova, K., Serov, A., Rojas-Carbonell, S. & Atanassov, P. Chemistry of Multitudinous Active Sites for Oxygen Reduction Reaction in Transition Metal–Nitrogen–Carbon Electrocatalysts. *J. Phys. Chem. C* **119**, 25917–25928 (2015).

157.   Chen, Y. *et al.* Catalysts by pyrolysis: Direct observation of transformations during re-pyrolysis of transition metal-nitrogen-carbon materials leading to state-of-the-art platinum group metal-free electrocatalyst. *Materials Today* **53**, 58–70 (2022).

158.   Huang, Y. *et al.* Catalysts by pyrolysis: Direct observation of chemical and morphological transformations leading to transition metal-nitrogen-carbon materials. *Materials Today* **47**, 53–68 (2021).

159.   Eisenberg, D., Slot, T. K. & Rothenberg, G. Understanding Oxygen Activation on Metal- and

Nitrogen-Codoped Carbon Catalysts. *ACS Catal.* **8**, 8618–8629 (2018).

160.   Wickramaratne, N. P. *et al.* Nitrogen Enriched Porous Carbon Spheres: Attractive Materials for

Supercapacitor Electrodes and CO2 Adsorption. *Chem. Mater.* **26**, 2820–2828 (2014).

161.   Khedekar, K. *et al.* Probing Heterogeneous Degradation of Catalyst in PEM Fuel Cells under

Realistic Automotive Conditions with Multi-Modal Techniques. *Advanced Energy Materials* **11**,

2101794 (2021).